

Dark matter in early–type galaxies: dynamical modelling of IC 1459, IC 3370, NGC 3379 and NGC 4105

S. Samurović^{1,2,3,4*} and I. J. Danziger^{2*}

¹*Dipartimento di Astronomia, Università di Trieste, Via Tiepolo 11, I-34131 Trieste, Italy*

²*INAF, Osservatorio Astronomico di Trieste, Via Tiepolo 11, I-34131 Trieste, Italy*

³*Astronomical Observatory, Volgina 7, 11160 Belgrade, Serbia and Montenegro*

⁴*Institute Isaac Newton of Chile, Yugoslavia Branch*

Accepted Received; in original form

ABSTRACT

We analyse long–slit spectra of four early–type galaxies which extend from ~ 1 to ~ 3 effective radii: IC 1459, IC 3370, NGC 3379 and NGC 4105. We have extracted the full line–of–sight velocity distribution (in the case of NGC 3379 we also used data from the literature) which we model using the two–integral approach. Using two–integral modelling we find no strong evidence for dark haloes, but the fits suggest that three–integral modelling is necessary. We also find that the inferred constant mass–to–light ratio in all four cases is typical for early–type galaxies. Finally, we also discuss the constraints on the mass–to–light ratio which can be obtained using X–ray haloes in the case of IC 1459, NGC 3379 and NGC 4105 and compare the estimated values with the predictions from the dynamical modelling.

Key words: galaxies: kinematics and dynamics — galaxies: elliptical, and lenticular — galaxies: structure – dark matter — galaxies: ISM — X–rays

1 INTRODUCTION

The problem of dark matter in galaxies remains perhaps the most important astrophysical problem in contemporary cosmology and extragalactic astronomy. Although its nature is still unknown, general but not unanimous opinion is that it exists and that it is a necessary ingredient of every viable cosmological model (see recent overview of the dark matter problem in galaxies in Binney 2004). The existence of the dark matter in spiral galaxies is rather clear mainly because of existence of cool gas which provides a powerful tool for obtaining rotation curves, that are, for most spirals, nearly flat thus indicating the presence of dark mass in their outer parts – dark haloes (see, e.g., Binney & Tremaine 1987 Sec 10.1). There are problems in the determination of its shape, but observations tend to conclude that the dark halo is flattened (see, e.g., Samurović, Ćirković & Milošević–Zdjelar 1999).

However, the problem of dark matter in elliptical galaxies (early–type galaxies, in general) is more complicated – it is more difficult to confirm the presence of dark haloes around ellipticals. Since elliptical galaxies contain little or no cool gas usually one cannot use 21–cm observations to trace kinematics of neutral hydrogen out to large radii, as is possible in the case of spirals. In an attempt to check

whether ellipticals have dark haloes one can use stellar kinematics, but since their outer parts are very faint, it is usually difficult to obtain spectra to constrain kinematics at large radii. An additional problem is related to the fact that one does not *a priori* know anything about the orbits of stars in ellipticals. Current investigations lead to the conclusion that there is less unambiguous evidence for the dark matter in ellipticals than in the case of spirals. Moreover, there are hints that in ellipticals the dark matter is not needed at all or, more precisely, not needed in some early–type galaxies, out to a given observed distance from the galactic centre (see, for example, Romanowsky et al. 2003).

The dark matter problem in elliptical galaxies can be studied using different tracers of mass: as in Danziger (1997) one can split the different methodological approaches into three large groups of tracers: gas, test particles and lensing methods. Without going into details about the features of all these groups we can note that the different methodologies provide different claims about the existence of the dark haloes in early–type galaxies. Here, we will constrain ourselves to the methods that provide data out to large radii (larger than $\sim 2\text{--}3R_e$, where R_e is the effective radius). The approach based on the study of the *hot gas* (X–ray haloes with temperature $T \sim 10^7$ K) (see a review in Mathews & Brighenti 2003) is based on two assumptions: (i) the gas obeys the perfect gas law and (ii) hydrostatic equilibrium holds. This method in general provides large mass–to–light

* E-mail: srdjan@ts.astro.it (SS); danziger@ts.astro.it (IJD)

ratios in the early-type galaxies (cf. Loewenstein & White 1999).

Some methods based on *test particles* include planetary nebulae, globular clusters and integrated stellar light. The *planetary nebulae (PNe)* method seems to be a very promising tool in dark matter research because PNe are detectable even in moderately distant galaxies through their strong emission lines. Méndez et al. (2001) studied 535 PNe in the flattened elliptical galaxy NGC 4697 and found that, assuming isotropic velocity distribution, this galaxy does not need dark matter interior to $3R_e$. Using the PNe method one derives mass-to-light ratios which are much lower than those derived using X-ray haloes: for example, Romanowsky et al. (2003) found for their sample (NGC 821 observed out to $3.5R_e$, NGC 3379 observed out to $\sim 5.5R_e$ and NGC 4494 observed out to $\sim 3R_e$) that velocity dispersion profiles show declines which indicates “the presence of little if any dark matter in these galaxies’ haloes”. Probably for NGC 3379 a better estimate of $R_e = 54.8$ arcsec is given by Capaccioli et al. (1990) and therefore the radial distance of $\sim 5.5R_e$ by Romanowsky et al. (based on RC3) should actually be $\sim 3.5R_e$. Here we adopt the Capaccioli et al. value for the effective radius of NGC 3379, see Sec. 3.3. This value was also used in the paper of Ciardullo et al. (1993), see below.

We have analyzed NGC 3379 below using long-slit spectra out to $2.2 R_e$ and found after a detailed dynamical modelling that there is no need to apply the dark matter hypothesis in order to obtain a successful fit for this galaxy. Peng, Ford & Freeman (2004) recently presented their results of an imaging and spectroscopic survey for PNe in NGC 5128. They found that PNe exist at distances out to 80 kpc ($\sim 15R_e$) making this study the most comprehensive kinematical study of an elliptical galaxy to date, both in the number of velocity tracers and in radial extent. They found that the dark matter is necessary to explain the observed stellar kinematics, but their value of M/L_B is low: within 80 kpc the total dynamic mass $\sim 5 \times 10^{11} M_\odot$ is found with $M/L_B \sim 13$. The problem with this method is that the h_3 and h_4 parameters which describe the the full line-of-sight velocity distribution (LOSVD) profile (see below) are not observationally determined as for the integrated spectra and an ambiguity about the mass distribution in the outer parts of galaxy may exist: strong tangential anisotropies can mimic the existence of the dark matter (Tonry 1983; Binney & Merrifield 1998 Sec 11.2).

The *globular clusters (GCs)* methodology can also be used in a search for dark matter. Côté et al. (2003) studied M49 (= NGC 4472) galaxy and showed that the radial velocities and density profiles of globular clusters provide “unmistakable evidence” for a massive dark halo interior to $\sim 3R_e$. Note again the problem of the estimate of the effective radius: Côté et al. determined $R_e = 186$ arcsec whereas RC3 gives $R_e = 104$ arcsec. This lower value of R_e would place their last measured point at $\sim 5.5R_e$. Recently, Bridges et al. (2003) presented their results obtained using Gemini/GMOS spectrograph of several early-type galaxies. It is important to note that they have observed 22 globular clusters in the aforementioned galaxy NGC 3379 and found no evidence of dark matter out to ~ 200 arcsec: in their preliminary analysis they reached the conclusion that the mass-to-light ratio *decreases* (from ~ 8 at ~ 60 arcsec to ~ 4 at ~ 200 arcsec, in the V-band). Richtler et al.

(2004) analyzed the GC system of the galaxy NGC 1399: they used 468 radial velocities assuming a pure Gaussian distribution to conclude that the velocity dispersion of this galaxy remains approximately constant between 2 and 9 arcmin (which corresponds to approximately 2.86 and 12.86 R_e) thus implying the existence of dark matter in this central galaxy of the Fornax cluster. The problem of the lack of the full LOSVD mentioned earlier still exists with this methodology.

A large set of dark matter investigations in early-type galaxies is made through studies of *integrated stellar light*. Because this paper deals with the two-integral (2I) approach we now focus on the papers that use this technique. Binney, Davies & Illingworth (1990) in their seminal paper established a 2I axisymmetric modelling based on the photometric observations. They analyzed galaxies NGC 720, NGC 1052, and NGC 4697 and modelled velocities and velocity dispersions out to $\sim 1 R_e$. van der Marel, Binney & Davis (1990) applied this approach to NGC 3379 (out to $\sim 1 R_e$), NGC 4261 (out to $\sim 1 R_e$), NGC 4278 (out to $\sim 1 R_e$) and NGC 4472 (out to $0.5 R_e$). Cinzano & van der Marel (1994) modelled the galaxy NGC 2974 out to $0.5 R_e$ introducing a new moment – modelling of the Gauss-Hermite moments (for definitions see below) defined previously in van der Marel & Franx (1993). Note however, that all these modelling procedures did not take into account dark matter, because they dealt with the regions in which dark matter was not expected to make a significant contribution. Saglia et al. (1993) presented kinematical and line strength profiles of NGC 4472, IC 4296 and NGC 7144 and from their dynamical modelling (quadratic programming) concluded that there is a strong evidence for dark matter in these galaxies. Carollo et al. (1995) observed and modelled a set of elliptical galaxies (NGC 2434, NGC 2663, NGC 3706 and NGC 5018). They used a 2I modelling procedure to model the stellar line-of-sight velocity distribution (using velocity dispersion and Gauss-Hermite h_4 parameter) out to two effective radii. They concluded that the massive dark matter haloes must be present in three of the four galaxies, and in the case of NGC 2663 there was no evidence of dark matter. Rix et al. (1997) used the Schwarzschild (1979) method for construction of axisymmetric and triaxial models of galaxies in equilibrium without explicit knowledge of the integrals of motion. They introduced into the analysis velocity, velocity dispersion and Gauss-Hermite parameters h_3 and h_4 . They used the galaxy NGC 2434 (from Carollo et al. 1995) to perform a detailed spherical dynamical modelling in order to conclude that this galaxy contains a lot of dark matter: they found that about half of the mass within one effective radius is dark.

Statler, Smecker-Hane & Cecil (1996) studied stellar kinematical fields of the post-merger elliptical galaxy NGC 1700 out to four effective radii. In a subsequent paper Statler, Dejonghe & Smecker-Hane (1999) found, using 2I axisymmetric models as well as three-integral (3I) quadratic programming models that NGC 1700 must have a radially increasing mass-to-light ratio, and that NGC 1700 “appears to represent the strongest stellar dynamical evidence to date for dark haloes in elliptical galaxies”. Statler & McNamara (2002) observed this galaxy in the X-ray domain and using gas modelling estimated the gas temperature to be ~ 0.5 keV. Note, however, that these authors found that probably

the hypothesis of hydrostatic equilibrium is not applicable in this case which would therefore make difficult the comparison between mass profiles based on the X-ray data and stellar dynamics. Saglia et al. (2000) modelled the galaxy NGC 1399 using 2I models (major photometric axis only) out to $\sim 2.5 R_e$. They marginally detected the influence of the dark component that starts from $1.5 R_e$.

Kronawitter et al. (2000) modelled a sample of 21 elliptical galaxies out to $1-2 R_e$: for three of them (NGC 2434, NGC 7507, NGC 7626) they found that models based on luminous matter should be ruled out. De Bruyne et al. (2001) modelled NGC 4649 and NGC 7097 using 3I quadratic programming method and found that in the case of NGC 4649 a constant mass-to-light ratio ($M/L_V = 9.5$) fit can provide good agreement with the data and that a marginally better fit can be obtained including 10 per cent of dark matter at $1.2 R_e$. In the case of NGC 7097 both kinematic and photometric data can be fitted out to $1.6 R_e$ using a constant mass-to-light ratio ~ 7.2 . Cretton, Rix & de Zeeuw (2000) modelled the giant elliptical galaxy NGC 2320 using the Schwarzschild orbit superposition method and found that the models with a radially constant mass-to-light ratio and logarithmic models with dark matter provide comparably good fits to the data and have similar dynamical structure (but note that the mass-to-light ratio in the V-band is rather large: ~ 15 for the mass-follows-light models and ~ 17 for the logarithmic models).

Finally, we mention the paper of Cappellari et al. (2002) in which the internal parts of one of the two galaxies which we analyze in this paper, IC 1459, were modelled using 3I axisymmetric technique.

From what is given above it is obvious that concerning the existence of dark matter in early-type galaxies the situation remains rather unclear: some appear to have dark matter haloes, and the others appear to be devoid of the dark component. One important note may be appropriate: recent observations that extend out to large radial distances from the centre ($> 5R_e$) (for example, PNe, GCs methodologies), although rare and incomplete (because of the lack of knowledge of the full LOSVD) strongly suggest that the evidence for the dark matter in these outer regions is scarce, and that the calculated mass-to-light ratios are small (either equal or marginally larger than those estimated in the inner regions). This is obviously at odds with values claimed from the X-ray observations. This study addresses, what we can call, “intermediate” regions out to $\sim 1-3R_e$ taking into account the full LOSVD.

In this paper we analyze in detail using 2I approach four early-type galaxies: IC 1459, IC 3370, NGC 3379 and NGC 4105 for which we have long-slit spectra that extend out to $\sim 1-3R_e$. In Sect. 2 we give some theoretical foundations related to both observational and modelling aspects. In Sect. 3 we briefly present the features of these four galaxies together with the photometric observations. Section 4 provides observational and data reduction information. 2I modelling results are given in Section 5. In Section 6 we compare the results obtained with the 2I technique with those obtained using X-ray haloes technique (in the case of IC 1459, NGC 3379 and NGC 4105). Finally, our conclusions are presented in Section 7.

2 THEORETICAL FOUNDATIONS

2.1 Line of sight velocity distributions

In the case of all external galaxies, one cannot obtain data necessary for the reconstruction of the distribution function of the stellar system directly: one can observe line-of-sight velocities and angular coordinates. Since individual stars cannot be resolved, one has to deal with integrated stellar light that represents the average of the stellar properties of numerous unresolved stars that lie along each line of sight (LOS). The first step in the analysis of the shifts and broadenings is to define the line of sight velocity distribution (LOSVD, also called velocity profile, VP): this is a function $F(v_{\text{LOS}})$ that defines the fraction of the stars that contribute to the spectrum that have LOS velocities between v_{LOS} and $v_{\text{LOS}} + dv_{\text{LOS}}$ and is given as $F(v_{\text{LOS}})dv_{\text{LOS}}$. Now, if one assumes that all stars have identical spectra $S(u)$ (where u is the spectral velocity in the galaxy’s spectrum), then the intensity that is received from a star with LOS velocity v_{LOS} is $S(u - v_{\text{LOS}})$. When one sums over all stars one gets:

$$G(u) \propto \int dv_{\text{LOS}} F(v_{\text{LOS}}) S(u - v_{\text{LOS}}). \quad (1)$$

This relation represents the starting point for a study of stellar kinematics in external galaxies (cf. Binney & Merrifield 1998 Sec 11.1). The observer obtains $G(u)$ for a LOS through a galaxy by obtaining its spectrum. If the galaxy is made of a certain type of star, one can estimate $S(u)$ using a spectrum of a star from the Milky Way galaxy.

One possible solution is to assume that the LOSVD has the Gaussian form. Sargent et al. (1977) invented the method known as Fourier Quotient Method, that has a problem of large errors for the ratio $\frac{\hat{G}(k)}{S(k)}$ that vary from point to point. The cross-correlation method based on the calculation of the cross-correlation function between the galaxy and the stellar spectra was pioneered by Simkin (1974) and developed further by Tonry and Davis (1979) and Statler (1995).

In this paper we model the LOSVD as truncated Gauss-Hermite (F_{TGH}) series that consists of a Gaussian that is multiplied by a polynomial (van der Marel & Franx 1993; also Gerhard 1993):

$$F_{\text{TGH}}(v_{\text{LOS}}) = \Gamma \frac{\alpha(w)}{\sigma} \exp\left(-\frac{1}{2}w^2\right) \left[1 + \sum_{k=3}^n h_k H_k(w) \right] \quad (2)$$

here Γ represents the line strength, $w \equiv (v_{\text{LOS}} - \bar{v})/\sigma$, $\alpha \equiv \frac{1}{\sqrt{2\pi}} \exp(-w^2/2)$, where \bar{v} and σ are free parameters. h_k are constant coefficients and $H_k(w)$ is a Gauss-Hermite function, that is a polynomial of order k . We will truncate the series at $k = 4$ (although higher values are also possible), for which the polynomials are:

$$H_0(w) = 1, \quad (3)$$

$$H_1(w) = \sqrt{w}, \quad (4)$$

$$H_2(w) = \frac{1}{\sqrt{2}}(2w^2 - 1), \quad (5)$$

$$H_3(w) = \frac{1}{\sqrt{6}}(2\sqrt{2}w^3 - 3\sqrt{2}w), \quad (6)$$

and

$$H_4(w) = \frac{1}{\sqrt{24}}(4w^4 - 12w^2 + 3). \quad (7)$$

It can be shown (van der Marel & Franx 1993) that $H_l(w)$ (in this case, $l = 0, \dots, 4$) are orthogonal with respect to the weight function $\alpha^2(w)$.

Now the LOSVD can be calculated by varying the values of \bar{v} , σ , h_3 and h_4 until the convolution of the function $F_{TGH}(v_{\text{LOS}})$ with a template star spectrum best reproduces the observed galaxy spectrum. The optimal fit is then reached using a non-linear least-squares fitting algorithm. If the form of the LOSVD is close to the Gaussian form, then \bar{v} and σ will be approximately equal to $\overline{v_{\text{LOS}}}$ and σ_{LOS} . Parameters h_3 and h_4 are important because they measure asymmetric and symmetric departures from the Gaussian. If one detects a positive (negative) value of the h_3 parameter that would mean that the distribution is skewed towards higher (lower) velocities with respect to the systemic velocity. On the other hand, if one detects $h_4 > 0$ this means that the distribution is more peaked than the Gaussian at small velocities with more extended high-velocity tails; for $h_4 < 0$ the distribution is more flat-topped than the Gaussian. In the study of the dark matter in the early-type galaxies the value of the h_4 parameter plays a crucial role because it is constraining the level of tangential anisotropy which is extremely important since it is well known that the excess of tangential motions can mimic the existence of the dark matter haloes in these galaxies (Danziger 1997; Gerhard 1993).

2.2 Two-integral (2I) modelling

For the 2I modelling procedures we used the modelling technique developed by Binney, Davies & Illingworth (1990, hereafter BDI), and subsequently used by van der Marel, Binney & Davies (1990) and Cinzano & van der Marel (1994). Only in Cinzano & van der Marel (1994) does the modelling include h_3 and h_4 parameters. These h_l models are based on the assumptions of Gaussian bulge and disk components. Statler et al. (1999) used the modified version of this method to analyze the mass distribution in NGC 1700. Here we present briefly the assumptions and the modelling steps.

2I modelling is the first step in understanding of the dynamics of the elliptical galaxies, because in cases of small departures from triaxiality (which is far more probable, and very strong in the case of IC 3370 as will be shown below), comparison of real systems with the models can provide useful insights. The assumptions of axisymmetry and the fact that the velocity dispersion tensor is everywhere isotropic are the starting points for the procedure that includes the following three steps (cf. BDI): (i) inversion of the luminosity profiles and obtaining three-dimensional luminosity density that provides the mass density (under the assumption of constant mass-to-light ratio); (ii) evaluation of the potential and derivation of the velocity dispersion and azimuthal streaming (under the assumptions that the form of the distribution function is $f(E, L_z)$, where E is the energy and L_z is the angular momentum of the individual star about the symmetry axis of the galaxy and that the velocity dispersion is isotropic as a starting point) and (iii) comparison of the projected kinematical quantities from the model with the observed kinematic parameters; optionally, a disc, and/or a

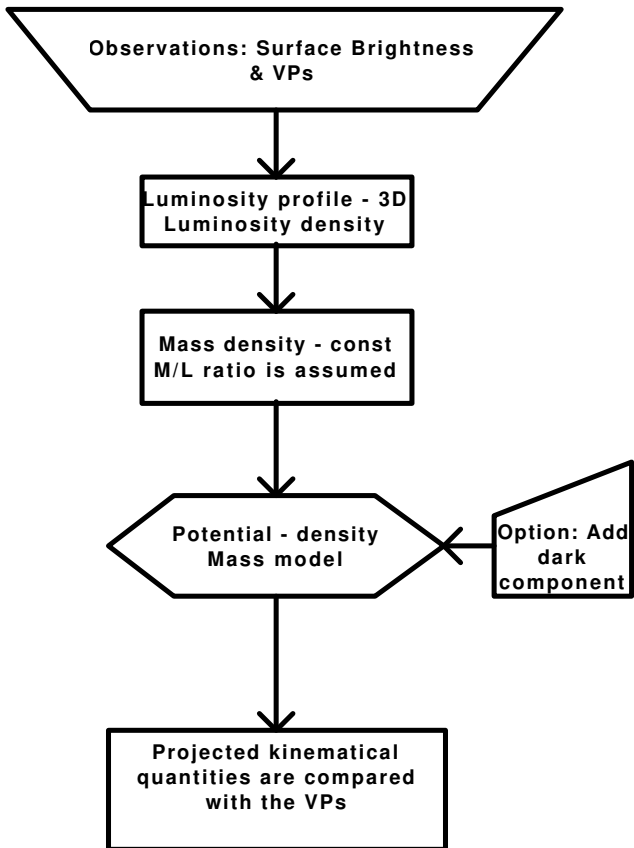


Figure 1. Flowchart of 2I modelling.

dark halo can be included in the modelling procedure. The flowchart of the modelling procedure is given in Fig. 1.

The first step in the modelling procedure involves making a least-squares fit for a flattened Jaffe model (Jaffe 1983, Eqs. (2) and (3)) or a flattened modified Hubble model. The brightness distribution in the case of the modified Hubble profile is given as (see Binney & Tremaine 1987, Eq. (2-39)):

$$I(R) = \frac{2j_0 a}{1 + (R/a)^2}, \quad (8)$$

(where j_0 is the central luminosity density and a is the core radius), and was used in the 2I modelling procedures of the two galaxies in this paper. Because we were mainly interested in the outer parts of galaxies we did not correct for the effects of seeing that are of importance near the centres of galaxies. Six Lucy iterations were used to get a fit of the surface brightness profile to the model. In cases when the disc was taken into account, the surface brightness of the disc was subtracted assuming that the disc is exponential.

For the evaluation of the dynamical quantities one assumes that the spheroid's mass density $\rho(R, z) = \Upsilon_s j(R, z)$ where Υ_s is some constant mass-to-light ratio, and $j(R, z)$ is the luminosity density. Here, it would be appropriate to present an estimate of the typical mass-to-light ratio in elliptical galaxies. van der Marel (1991) found in his sample of 37 bright ellipticals that the average mass-to-light ratio in the B -band is: $M/L_B = (5.95 \pm 0.25)h_{50}$ thus $M/L_B = 8.33 \pm 0.35$ for $h_0 = 0.70$. He also found that the mass-to-light ratio is correlated with the total lu-

minosity: $M/L_B = 3.84h_{50}(L_B/L_{*,B})^{0.35}$, where $L_{*,B} \equiv 3.3 \times 10^{10} h_{50}^{-2} L_\odot$.

The details related to the 2I modelling procedure which we use are given in BDI and Cinzano & van der Marel (1994) and Fig. 1. Below we give some of the most important steps.

Since we assume in this paper that the distribution function is of the form $f(E, L_z)$ the second radial velocity moment, $\overline{v_R^2} \equiv \sigma_R^2$, and the second vertical velocity moment, $\overline{v_z^2} \equiv \sigma_z^2$ are everywhere equal and $\overline{v_R v_z} \equiv 0$. Solving the Jeans equations we search for unknowns $\overline{v_\phi^2}$ and $\sigma_R^2 = \sigma_z^2$. Using a free parameter, k , one can, as usual, assign a part of the second azimuthal velocity moment $\overline{v_\phi^2}$ to streaming:

$$\overline{v_\phi} = k \sqrt{\overline{v_\phi^2} - \sigma_R^2}. \quad (9)$$

Then we project the dynamical quantities on to the sky to obtain predictions, always taking into account a given inclination angle i (which is a free parameter given at the beginning of the 2I procedure): this is an angle measured from the galaxy's rotation axis to the line-of-sight: for edge-on galaxy $i = 90^\circ$ and for face-on galaxy $i = 0^\circ$. We always start the modelling with the value $k = 1$ which is a natural starting point, because it implies an isotropic dispersion vector.

For the modelling of the stellar kinematics we used freely available ‘‘Two-integral Jeans modelling Software’’ made by R. van der Marel and J. Binney, again on the x86 GNU/Linux PC platform (see the comment about the software used for the extraction of the kinematics above).

3 GENERAL INFORMATION AND PHOTOMETRIC OBSERVATIONS

In all the analyses that we are performing we assume that the Hubble constant is equal to $70 \text{ km s}^{-1} \text{ Mpc}^{-1}$. The standard steps were performed in the data reduction of the photometric observations of IC 1459 and IC 3370: bias subtraction, flat-fielding, cleaning of cosmic rays and subtraction of sky background. We used the IRAF¹ task ELLIPSE to extract the full photometric profiles in both cases.

3.1 IC 1459

IC 1459 is a giant E3 elliptical galaxy. Its absolute blue magnitude is -20.52 , heliocentric radial velocity 1691 km s^{-1} (taken from NED database and in agreement with our observations). It covers 5.2×3.8 arcmin on the sky (RC3). One arcsec in the galaxy corresponds to ~ 117.16 pc. The effective radius is 33 arcsec ($=3.87$ kpc). One of its most characteristic features is a fast counterrotating stellar core (Franx & Illingworth 1988). It has other peculiarities: twisted isophotes (Williams & Schwarzschild 1979), a dust lane and patches near the nucleus (Sparks et al. 1986) and an ionized gaseous disc at the core that rotates along the major axis in the same direction as the majority of stars in the galaxy – this is the opposite direction to that of the stellar core (Forbes, Reizel & Williger 1995). The nucleus of

IC 1459 has a strong (1Jy) compact radio source (Slee et al 1994). Recently, Fabbiano et al. (2003) observed this galaxy with *Chandra* ACIS-S: these observations will be used below, when comparing stellar dynamics and X-ray data.

Verdoes Kleijn et al. (2000) analyzed kinematical observations of the nuclear gas disc, and found a central black hole of mass $M_{\text{BH}} = (2 - 6) \times 10^8 M_\odot$. Cappellari et al. (2002) observed IC 1459 using several slit positions and constructed axisymmetric 3I models of this galaxy using the Schwarzschild orbit superposition method. They found, using stellar and gas kinematics, that $M_{\text{BH}} = (1.1 \pm 0.3) \times 10^9 M_\odot$. The mass-to-light ratio found in this paper was ~ 8.8 (when converted to the B -band and the distance used in this paper, $D = 24.16$ Mpc) and is in agreement with our estimate (we found that $M/L = 5 - 10$).

3.1.1 Photometric observations

Photometric observations were made by one of us (IJD) during 1997 August 28–30 using the ESO NTT and EMMI in the Red Medium Spectroscopy mode in the V -band. We present the results obtained using the aforementioned IRAF routine in Fig. 2 (left) where surface brightness was transformed to the B -band using relation $B - V = 0.99$ taken from the LEDA² database. The photometric profile was compared with that of Franx & Illingworth (1988) and it was found that it was in a good agreement.

3.2 IC 3370

IC 3370 is a bright galaxy, classified as E2–E3 (elliptical) galaxy, absolute blue magnitude -21.4 , heliocentric radial velocity 2930 km s^{-1} (taken from NED database and in agreement with our observations). It covers 2.9×2.3 arcmin on the sky (RC3). However, it is a rather unusual elliptical galaxy and according to Jarvis (1987, hereafter referred to as J87) it should be classified as S0pec (see below). One arcsec in the galaxy corresponds to ~ 203.02 pc. The effective radius is 35 arcsec ($=7.10$ kpc).

3.2.1 Photometric observations

We used frames kindly provided by O. Hainaut using ESO NTT and EMMI in the RILD mode on July 3–4, 2002 in the B -band. The photometry of IC 3370 is very interesting and it is given in detail in J87. We present here some additional elements that are complementary to that study and are of importance for the analysis that we are undertaking.

One should note that J87 took for the major axis the position angle (PA) of 40° , Carollo, Danziger & Buson (1993) took for the same axis P.A. of 51° , while the spectra in this study were taken using P.A. = 60° . The reason for these differences lies in a very particular photometry of this galaxy that has strong isophotal twisting as shown in J87 and in Fig. 2 (see position angle (P.A.) plot). This may be evidence for the fact that this galaxy is triaxial, because the isophotes of an axisymmetric system must always be aligned with one another (see, for example, Binney & Merrifield 1998 Sec 4.2).

¹ IRAF is distributed by NOAO, which is operated by AURA Inc., under contract with the National Science Foundation.

² <http://leda.univ-lyon1.fr/>.

Fasano & Bonoli (1989) using a sample of 43 isolated ellipticals found that the twisting observed in these galaxies is intrinsic (triaxiality). Jarvis has taken the mean position angle of isophotes to be equal to $40 \pm 2^\circ$ which is true for the data up to 80 arcsec. However, at larger radii the P.A. tends to increase, so the usage of larger value of 60° (and 150° for the minor axis) is justified (see Fig. 2).

In Fig. 2 (right) we present relevant photometric data obtained using IRAF task ELLIPSE: ellipticity, magnitude in the B -band for major axis (filled circles) and minor axis (open circles), a_4 parameter (which measures the fourth Fourier component of the intensity variations along the best-fitting ellipse to an isophote) and the position angles, as a function of distance. The value of a_4 is positive up to one effective radius (for almost all values of radius), thus indicating that the isophotes are discy, while beyond one effective radius, the isophotes become boxy since a_4 is negative. Since a_4 increases rapidly up to ~ 5 arcsec this can lead to the conclusion of the embedded disc. The existence of the stellar disc was shown in J87.

3.3 NGC 3379

NGC 3379 is a bright E1 galaxy (note the ellipticity $\epsilon \approx 0.15$ in Fig. (3) (left)); there are still some doubts whether this is a bona fide normal elliptical or a face-on lenticular galaxy (Statler 2001; Gregg et al. 2004 Sec 7), with a heliocentric radial velocity of 911 km s^{-1} , (taken from the NED database) and absolute B magnitude -20.57. One arcsec in the galaxy corresponds to ~ 63.12 pc. The effective radius is 54.8 arcsec ($=3.46$ kpc); see also the discussion in Introduction. Its kinematics have been the subject of several papers by Statler and collaborators (Statler 1994; Statler & Smecker-Hane 1999; Statler 2001).

3.3.1 Photometric observations

The surface brightness was taken from the paper of Capaccioli et al. (1990), whereas ellipticity, a_4 parameter and position angle as function of radius were extracted from images from the ESO archive (I -band, NTT SUSI) using standard IRAF commands. This galaxy shows small departures of a_4 parameter from zero beyond ~ 2 arcsec. The position angle is approximately constant beyond ~ 15 arcsec.

3.4 NGC 4105

NGC4105 is an E2 galaxy, with heliocentric radial velocity of 1918 km s^{-1} (taken from the NED database), and absolute B magnitude -20.72. One arcsec in the galaxy corresponds to ~ 134.14 pc. The effective radius is 35 arcsec ($=4.69$ kpc).

NGC 4105 belongs to a binary system with a companion galaxy NGC 4106. which is ~ 1 arcmin away from NGC 4105. Longhetti et al. (1998) claimed to see evidence of the interaction in the velocity profiles of NGC 4105. In their study they used the position angle of 118 degrees to find asymmetric profiles for both velocity and velocity dispersion. In our study we used position angle of the major photometric axis of 150 degrees and of the minor photometric axis of 60 degrees. For these position angles we notice departures from symmetry, but since the effect is not so

strong out to $\sim 1R_e$ (most notably for the velocity dispersion and the h_4 parameter, for the major axis, see Sec. 4.4 below) in the following discussion we will neglect the possible gravitational influence of NGC 4106.

3.4.1 Photometric observations

Photometric data were extracted from frames obtained courtesy of M. Carollo & K. Freeman (who used ESO 2.2 m telescope with EFOSC) using standard IRAF routines. The photometric profiles are given in the R -band. We present the results obtained using the IRAF routines in Fig. 3 (right). Beyond ~ 6 arcsec the position angle is approximately constant. Photometry of NGC 4105 has been presented in Reduzzi & Rampazzo (1996): our photometric profiles are in a good agreement with the results presented in this paper.

We present the basic data related to IC 3370, IC 1459, NGC 3379 and NGC 4105 with the data sources in Table 1. Note that for IC 3370 because of the fact that the X-ray was not detected the estimates based on the X-ray data are missing (see Sec. 6 for details).

4 STELLAR KINEMATICS

Long-slit spectra observations of IC 1459 and IC 3379 were made by one of us (IJD) during 1997 August 28–30 using the ESO NTT and EMMI in the Red Medium Spectroscopy mode. The central wavelength was chosen to be near the Mg_2 feature: $\sim 5150 \text{ \AA}$. The range that was covered was $\sim 700 \text{ \AA}$. The spectra were rebinned at the telescope over 2 pixels giving a scale of $0.56 \text{ arcsec pixel}^{-1}$. The spectroscopic observations of NGC 3379 and NGC 4105 were obtained courtesy of M. Carollo and K. Freeman. Galaxy NGC 3379 was observed using the Double Beam Spectrograph attached to the Australian National University 2.3 m telescope at Siding Springs Observatory. NGC4105 was observed using ESO 2.2 m telescope with EFOSC. The central wavelength was the Mg_2 feature: $\sim 5150 \text{ \AA}$. The range covered was $\sim 1000 \text{ \AA}$ (for NGC 3379) and $\sim 1200 \text{ \AA}$ (for NGC 4105).

The standard data reduction steps were performed for all the galaxies: bias subtraction, flat-fielding, cleaning of cosmic rays and subtraction of sky background. We used the MIDAS³ package in which we implemented several routines necessary for fast reduction (wavelength calibration) and post-reduction procedures (logarithmic binning of the spectra). Wavelength calibration was done using the Helium–Argon (for IC 1459, IC 3370, NGC 4105) and Neon–Argon (for NGC 3379) comparison lamps spectra. Sky subtraction was done by taking an average of 30 rows near the edges of the exposure frames. Finally the spectra were rebinned on a logarithmic scale. Also, spectra of several template stars were reduced as described above, continuum divided, and averaged over several rows in order to obtain one stellar template spectrum of high signal-to-noise ratio (S/N).

For the extraction of the stellar kinematics we used freely available ‘‘Gauss–Hermite Fourier Fitting Software’’ made by R. van der Marel and M. Franx. Since this package

³ MIDAS is developed and maintained by the European Southern Observatory.

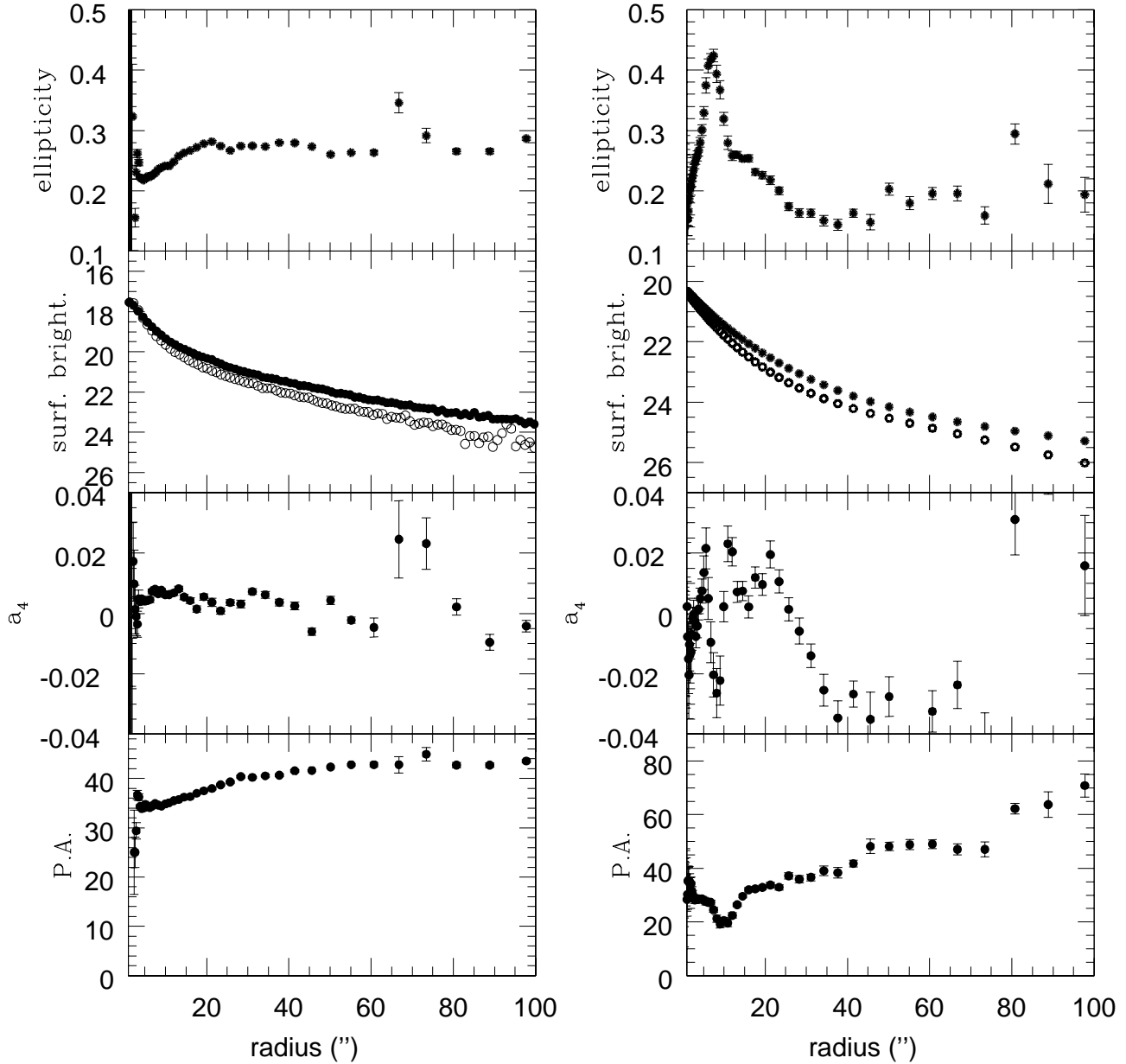


Figure 2. Photometric profiles of IC 1459 and IC 3370. *Left:* Photometric profiles for IC 1459 (in the V -band). From top to bottom: ellipticity, surface brightness for the B filter (see text) in mag arcsec^{-2} (for major axis: full circles; for minor axis: open circles), a_4 parameter and position angle. *Right:* Photometric profiles for IC 3370 (in the B -band). From top to bottom: ellipticity, surface brightness in mag arcsec^{-2} (for major axis: full circles; for minor axis: open circles), a_4 parameter and position angle.

was written for the Sun FORTRAN compiler for the Sun UNIX platform, initial testing was done using Sun Sparc (Sun-Blade-100) platform. Later, it was modified and ported to the x86 GNU/Linux PC platform that uses a GNU FORTRAN compiler. Detailed tests were done, and it was found that the results obtained in two different environments were in the excellent agreement. All the results presented in this paper were obtained in the GNU/Linux environment.

4.1 IC 1459

Several exposures were taken for two different position angles: for the galactic major axis (P.A. = 40°) total exposure of 35,100 s, and for the minor axis (P.A. = 130°) total exposure of 3,600 s. Because of the fact that only one exposure was available for the minor axis, the removal of the cosmic ray hits was not successful and we have taken the minor axis stellar kinematics from Cappellari et al. (2002). We compared the results for the major axis and plot the

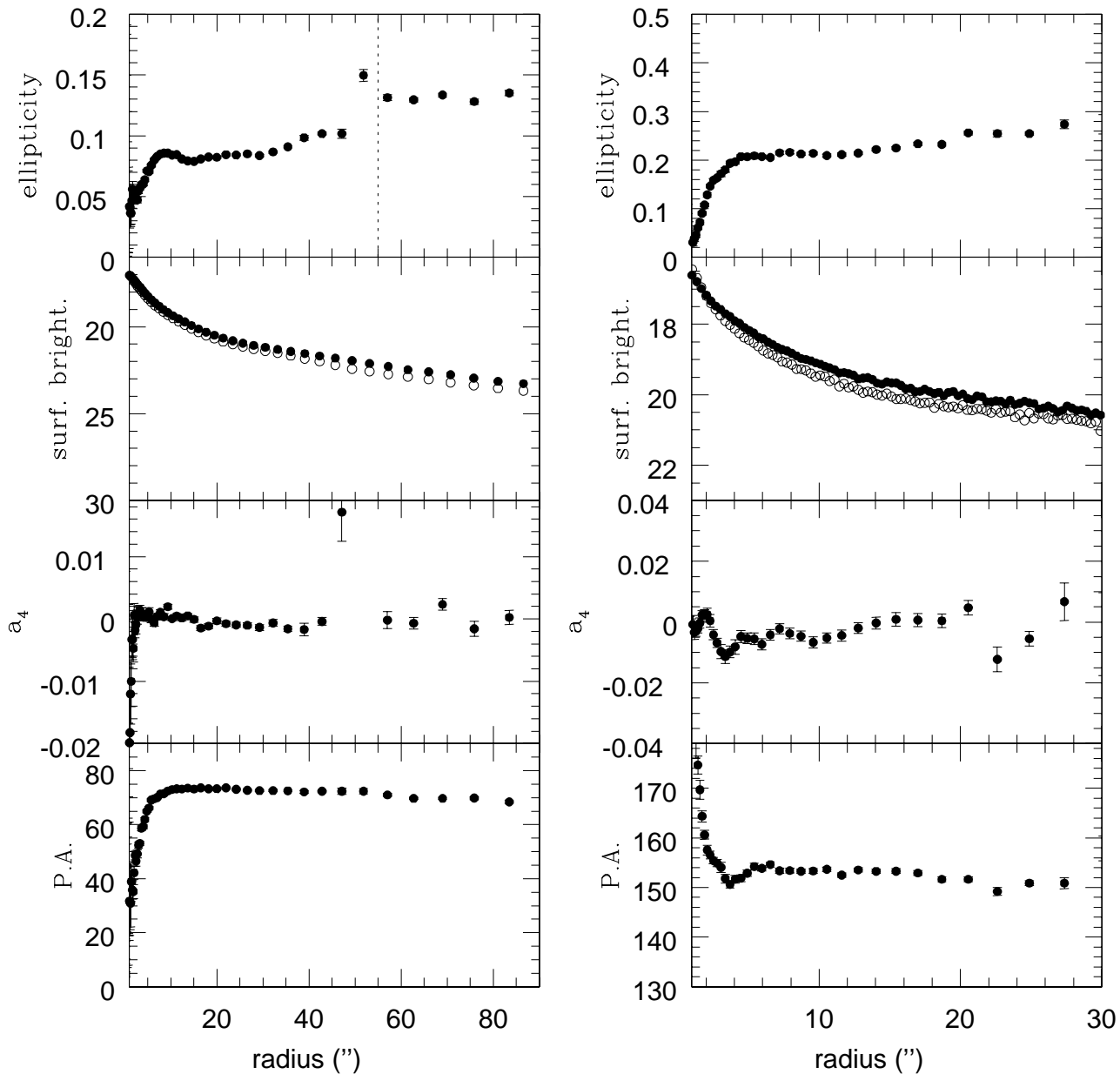


Figure 3. Photometric profiles of NGC 3379 and NGC 4105. Vertical dotted line indicates one effective radius (in the case of NGC 3379 only). *Left:* Photometric profiles for NGC 3379 in the I-band. From top to bottom: ellipticity, surface brightness (for the R filter from Capaccioli et al. (1990)) in mag arcsec^{-2} (for major axis: full circles; for minor axis: open circles), a_4 parameter (fourth harmonic deviations from ellipse) and position angle. *Right:* Photometric profiles for NGC 4105 (in the R-band). From top to bottom: ellipticity, surface brightness in mag arcsec^{-2} (for major axis: full circles; for minor axis: open circles), a_4 parameter and position angle.

comparison in Fig. 4 (left panel). The agreement is good, except for the velocity and h_3 parameter near the galactic centre where some discrepancy exists. Note, however, that Cappellari et al. (2002) used $\text{P.A.}=39^\circ$ and observations which we analyze here were made at $\text{P.A.}=40^\circ$. In the outer parts agreement is excellent for the whole velocity profile. The template star HR 5582 (type K3⁻) was used. The instrumental dispersion was $\sim 3.5 \text{ \AA}$ ($\sim 190 \text{ km s}^{-1}$) and

was determined using Helium–Argon spectrum in a region $\sim 5000 \text{ \AA}$. The slit width was 3 arcsec.

In Fig. 4 (middle and right panel) we show the major and minor axis kinematic parameters. Major axis data show the rapid increase of velocity in the inner ~ 3 arcsec: velocity rises to $\sim 100 \text{ km s}^{-1}$ (note however a small asymmetry in our determination of velocity). Velocity dispersion is large at the centre: $\sim 350 \text{ km s}^{-1}$, and decreases rapidly to $\sim 240 \text{ km s}^{-1}$ (at ~ 40 arcsec). There is a plateau in velocity dis-

Table 1. Basic properties of IC 1459, IC 3370, NGC 3379 and NGC 4105

Name	r [arcsec]	r [kpc]	r/R_e	B	$\log L_X$	T	D	M	$(\frac{M}{L})_B$
(1)	(2)	(3)	(4)	(5)	(6)	(7)	(8)	(9)	(10)
IC 1459	100	11.7	2.86	11.14	41.19	0.60	24.16	3.91	13.00
IC 3370	120	24.36	3.43	11.59	–	–	41.86	–	–
NGC 3379	80	5.04	1.46	10.10	39.78	0.26	13.01	0.92	7.00
NGC 4105	30	4.02	0.86	11.27	41.94	0.76	27.66	1.70	10.80

NOTES – Col. (2): radius out to which long-slit spectra extend (in arcsec). Col. (3): same as Col. (2) but in kpc. Col. (4): same as Col. (2) but in units of R_e . Col. (5): total B magnitude (taken from LEDA). Col. (6): X-ray luminosity (taken from: Brown & Bregman 1998 for IC 1459, Brown & Bregman 1998 for NGC 3379 and Fabbiano, Kim & Trinchieri 1992 for NGC 4105). Col. (7): temperature (taken from: Fabbiano et al. 2003 and Davis & White 1996 for IC 1459, Brown & Bregman 2001 for NGC 3379 and Davis & White 1996 for NGC 4105). Col. (8): distance calculated using $H_0 = 70 \text{ km s}^{-1} \text{ Mpc}^{-1}$ (using heliocentric radial velocities from the NED archive). Col. (9): mass in units of $10^{11} M_\odot$ estimated using Eq. (16) for the radius given in the Col. (2). Col. (10): estimate of the mass-to-light ratio using Eq. (17) again for the radius in the Col. (2). See Fig. 12 for estimates for IC 1459 based on other temperatures.

persion between ~ 20 arcsec and 30 arcsec after which velocity dispersion decreases. The h_3 parameter shows a typical behaviour, i.e. it rises (falls) when velocity rapidly increases (decreases). In the outer parts it shows small departures from zero. The h_4 parameter shows very small departures from zero in the inner parts, and in the outer parts there is an increase of its value, suggesting existence of the radial anisotropy. Minor axis data provide evidence of small velocities, and larger central velocity dispersion ($\sim 380 \text{ km s}^{-1}$). Both the h_3 and h_4 parameters show very small departures from zero throughout the observed parts of the galaxy.

4.2 IC 3370

Several exposures were taken for three different position angles: for the galactic major axis (P.A. = 60°) total exposure of 21,600 s, for the minor axis (P.A. = 150°) total exposure of 7,200 s. Also, the spectra of the intermediate axis were taken (P.A.= 20°), and the total exposure time was 14,400 s. The template star spectrum of HR 2701 (type K0III) was used. The instrumental dispersion was $\sim 3.5 \text{ \AA}$ ($\sim 190 \text{ km s}^{-1}$) and was determined using a Helium–Argon spectrum in a region $\sim 5000 \text{ \AA}$. The slit width was 3 arcsec.

In Fig. 5 (left panel) we show the major axis kinematic parameters. This galaxy indeed shows behaviour that is characteristic for an S0 galaxy: for example, its major axis kinematics can be compared to that of NGC 1461, lenticular galaxy from the Fisher (1997) sample. Note the usual behaviour of h_3 parameter: when the velocity rises, h_3 decreases, and vice versa. In Fig. 5 we present intermediate (middle panel) and minor (right panel) axis kinematic profiles: IC 3370 has minor axis rotation that provides an additional hint (apart from the isophotal twist) of the triaxiality. Note the small values (consistent with zero) of h_3 and h_4 at the large distances from the centre for the major axis and their generally small values in the case of the minor axis – they provide evidence of the lack of excessive tangential motions, that may mimic the dark matter in the outer parts of the galaxy (see above). In the case of the intermediate axis beyond 60 arcsec we have a hint of negative values of the h_4 parameter which could mimic dark matter in these regions.

4.3 NGC 3379

For NGC 3379 the long slit spectra of the major axis (P.A.= 70°) were taken on March 13-14, 1997 and the total exposure time was 6,000 s. The scale was 0.59 arcsec pixel $^{-1}$ and the wavelength calibration was done using a Neon-Argon lamp. The template star was K-giant cpd-43. The instrumental dispersion was $\sim 2 \text{ \AA}$ ($\sim 100 \text{ km s}^{-1}$) and was determined using a Neon-Argon spectrum in a region $\sim 5000 \text{ \AA}$. Slit width was 1.5 arcsec. Since we had only major axis (P.A.= 70°) data, which we reduced, we have taken data from Statler & Smecker-Hane (1999) for the major and the minor axis (P.A.= 340°). We compared the results for the inner region which we have in common for the major axis and found that they are in an excellent agreement (see Fig. (6 (left))). The data that we had extend out to ≈ 30 arcsec, so in the modelling procedures (see next Section) we will use Statler & Smecker-Hane (1999) measurements only at all radii because their data extend to a larger radius (80 arcsec that is $\approx 1.46 R_e$) and are also available for the minor axis.

This galaxy shows a steep increase of velocity: it rises to $\sim 60 \text{ km s}^{-1}$ in the inner 20 arcsec. After a plateau between ~ 20 arcsec and ~ 60 arcsec the velocity shows a tendency to decrease. The velocity dispersion peaks at $\sim 230 \text{ km s}^{-1}$ and then decreases rapidly. There is a plateau between ~ 20 arcsec and ~ 50 arcsec. One can see that there is an obvious asymmetry at ~ 80 arcsec. The h_3 parameter is small out to ~ 50 arcsec, but shows departures from zero at ~ 70 arcsec. h_4 remains small throughout the whole observed galaxy, except in the outer parts for which there is a hint of departures from zero, but since error bars are large, it is difficult to draw firm conclusions. Minor axis data suggest that NGC 3379 does not show significant rotation on the minor axis. The velocity dispersion profile is similar to that of the major axis. The h_3 and h_4 parameters are small throughout the whole observed galaxy on the minor axis (see Fig. 6).

4.4 NGC 4105

Long slit spectra of NGC 4105 were obtained on March 9-13, 1994 using the ESO 2.2 m telescope with EFOSC. The total

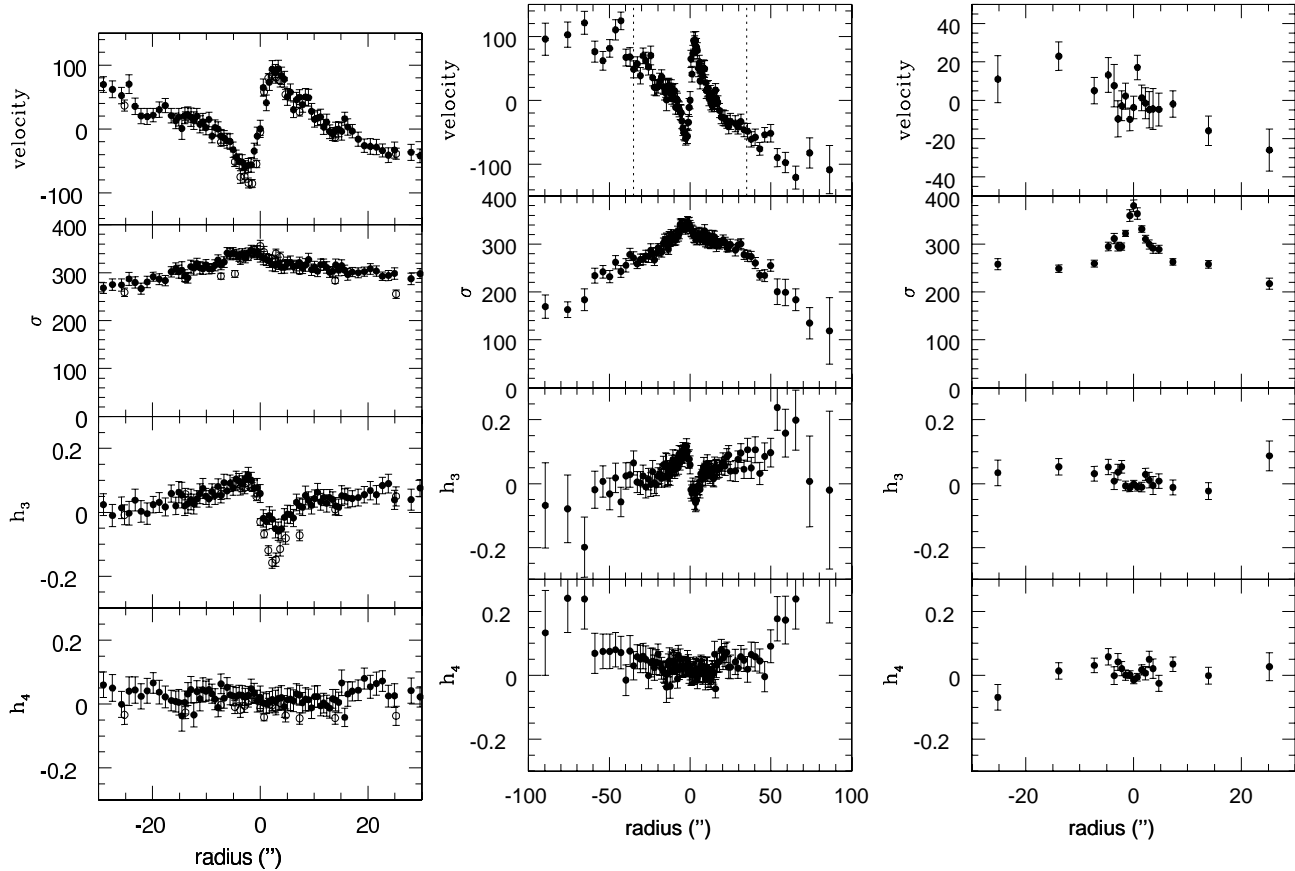


Figure 4. Stellar kinematics of IC 1459. *Left:* Comparison of the kinematic profiles for the major axis of IC 1459 (P.A.= 40°, black circles) and the data taken from Cappellari et al. (2002) (P.A.= 39°, open circles). *Middle:* major axis data. *Right:* minor axis data (taken from Cappellari et al. 2002). From top to bottom: velocity, velocity dispersion, h_3 and h_4 parameters. One effective radius in case of the major axis is plotted using dashed line. Note that in case of the minor axis it is out of scale.

exposure time for the major axis (P.A.=150°) was 27,900 s. The total exposure time for the minor axis (P.A.=60°) was 14,400 s. The scale was 0.336 arcsec pixel⁻¹. The wavelength calibration was made using a Helium–Argon lamp. The template star was HR 5582 (type K3⁻). The instrumental dispersion was $\sim 4.2 \text{ \AA}$ ($\sim 280 \text{ km s}^{-1}$) and was determined using Helium–Argon spectrum in the region near 5000 \AA . Slit width was 1.5 arcsec.

On the major axis this galaxy shows a maximum value of the velocity $\sim 60 \text{ km s}^{-1}$ (see Fig. 7, left). Note that there is a hint of a counterrotating stellar core in the inner 3 arcsec. In general, there is a lack of symmetry about the galaxy centre. The central value of the velocity dispersion is large: $\sim 320 \text{ km s}^{-1}$. It declines in the inner ~ 5 arcsec after which there is a tendency to remain constant (out to $0.7R_e$). The velocities are not antisymmetric: the reason for this could be the vicinity of NGC 4106 and interaction with it. h_3 also shows a hint of the effects of the counterrotating stellar core in the inner 3 arcsec. At the larger radii the value of h_3 is consistent with zero. The h_4 parameter remains small (slightly negative, but consistent with zero) throughout the whole observed galaxy. On the minor axis NGC 4105 shows rather complex behaviour and again a lack of symmetry is evident (see Fig. 7, right). The velocity dispersion decreases

from the central value of $\sim 320 \text{ km s}^{-1}$ to $\sim 200 \text{ km s}^{-1}$. Not much can be said about h_3 and h_4 parameters, except that they show asymmetries.

5 TWO-INTEGRAL (2I) MODELLING

In all the dynamical modelling performed below we folded the major axis data about the y -axis and the minor axis data were folded about x -axis. We took the mean value of the observed kinematical parameters in all the cases taking into account that the velocity and the h_3 parameter are odd functions and the velocity dispersion and the h_4 parameter are even functions of the radius. In the modelling which follows, we tested different inclinations for all the galaxies and we present here only the best-case inclinations.

5.1 IC 1459

This galaxy has a counterrotating core, and therefore, two-integral axisymmetric modelling conceived by BDI based on the photometric profiles will necessarily fail in the inner regions. We tested the inclination angles from 50° to 90° and we decided to use the inclination angle of 65° in all the cases

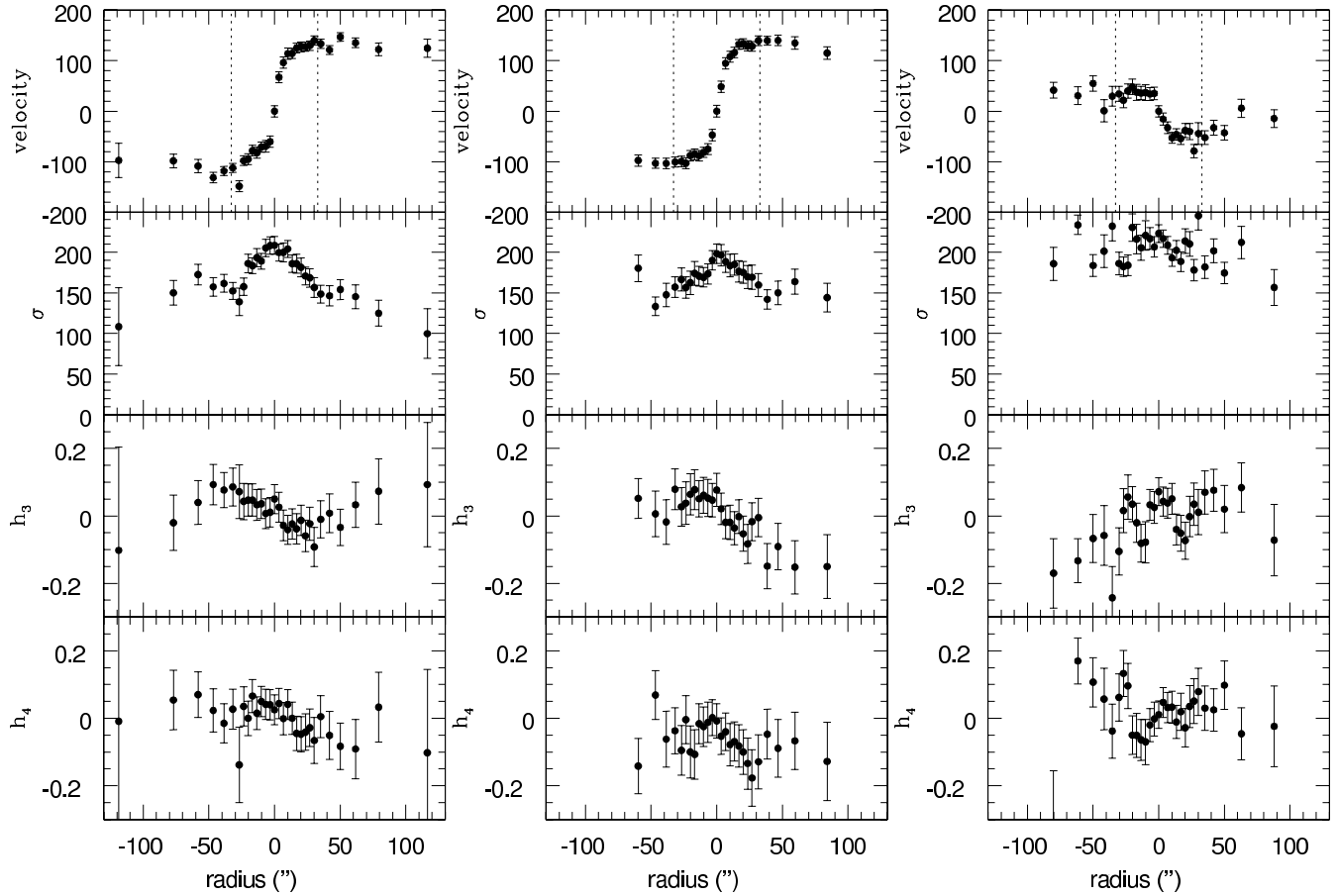


Figure 5. Kinematic profiles for major axis (P.A.= 60°, left), the intermediate (P.A.= 150°, middle) and minor (P.A.= 20°, right) axes of IC 3370. From top to bottom: velocity, velocity dispersion, h_3 and h_4 parameters. One effective radius is plotted using dashed lines.

because it provided the best fit to the data (although very far from perfect). This inclination angle implies intrinsic axis ratio of ~ 0.7 .

Major axis (Fig. 8(left)): In the case of the major axis we tested $k = 0.6$ value: first, it gave marginally good fit for the velocity in the outer region of the galaxy ($M/L_B = 3.81$), and a marginally good fit in the region slightly beyond $1R_e$ for the velocity dispersion (dashed line), and, second, a case of larger $M/L_B = 6.83$ did not fit the velocity, nor the velocity dispersion (dotted line). In both of these cases no dark matter halo was included, and no embedded disc was assumed. If one takes $k = 1$, there are two cases that we decided to present: first, $M/L_B = 6.83$ (no dark halo, and no embedded disc) (solid lines) the velocity is extremely large (it declines from $\sim 350 \text{ km s}^{-1}$ at 20 arcsec to $\sim 220 \text{ km s}^{-1}$ at 100 arcsec); the velocity dispersion can be fitted, very closely, throughout the whole observed galaxy, and second, the case when $M/L_B = 3.81$ (no dark halo, and no embedded disc) (dot-dashed lines) for which the fitted velocity has smaller values (although still much larger than the observed ones): in a region between 20 arcsec and 100 arcsec the velocity decreases from 260 km s^{-1} to 170 km s^{-1} ; the velocity dispersion is much lower, and the successful fit is attained only in the outer parts. The h_3 parameter, because of the fact that there is a counterrotating core, cannot be fitted. For the h_4 parameter this modelling did not give a successful fit in the outer parts where there possibly exists a radial

anisotropy (judging from the observed non-zero value of the h_4 parameter). Therefore, one can state that only the test with $k = 1$ ($M/L_B = 6.83 \pm 0.13$) can provide a fit to the velocity dispersion. The fact that the predicted velocity is much larger is of a crucial importance and will be addressed below.

It was argued that the Gauss–Hermite estimates are not the best approximation of the mean line-of-sight velocity and velocity dispersion of the LOSVD (cf. van der Marel & Franx 1993; Statler et al. 1996; De Rijcke et al. 2003), because their real values depend on the h_3 and h_4 parameters. In the case of IC 1459 there are significant departures in the Gauss–Hermite parameters from zero for a major axis so we applied the correction for the velocity and velocity dispersion. Following van der Marel & Franx (1993) we used the following formulas to get the corrected values that are then compared with the modelling results. The corrected values are, for the velocity:

$$v_{\text{corr}} = v_{\text{GH}} + \sqrt{3}(h_3)_{\text{GH}}\sigma_{\text{GH}}, \quad (10)$$

and for the velocity dispersion:

$$\sigma_{\text{corr}} = \sigma_{\text{GH}}(1 + \sqrt{6}(h_4)_{\text{GH}}), \quad (11)$$

where the index “GH” is related to the Gauss–Hermite estimates. This correction is done only in the case of the major axis, since in the case of minor axis the departures from zero in h_3 and h_4 are minimal. Using the Cinzano & van der

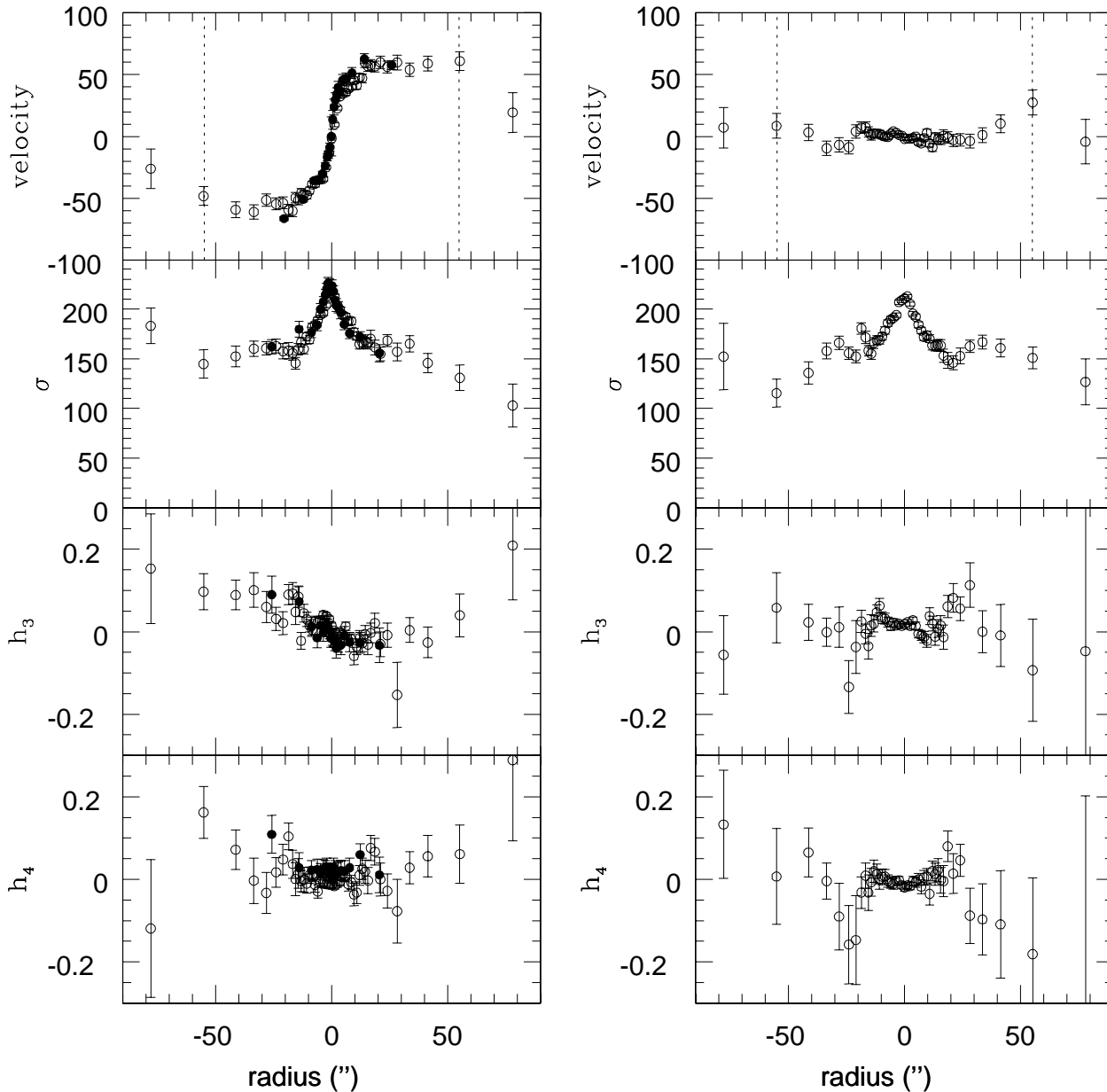


Figure 6. Open circles: stellar kinematics of NGC 3379 (taken from Statler & Smecker-Hane (1999)) for major (left) and minor (right) axis. Black circles: our extraction of the stellar kinematics given for comparison. From top to bottom: velocity, velocity dispersion, h_3 and h_4 parameters. Dashed line indicates one effective radius.

Marek modelling technique we did not correct the observed data in the inner regions (interior to ~ 6 arcsec) where the disc may be present and we corrected velocity and velocity dispersion beyond ~ 6 arcsec in order to compare with the models. In this inner region the model LOSVD is a sum of 2 Gaussians, and the modelled velocity dispersion is the physical velocity dispersion which is then compared to the data. We note that the non-zero values of the h_3 and h_4 parameters are not fitted because in the outer regions the models assume Gaussian LOSVDs. After the correction is done one can note the following change with respect to the

uncorrected values (see Fig. 8 (right panel)): the velocity dispersion values in the outer part have increased (h_4 is positive), but the general trend of decline remains. When one now examines the modelling results given in Fig. 8 (right panel) one can see that a better fit to the observations is obtained using $k = 0.6$, and the constant mass-to-light ratio $M/L_B = 5.31 \pm 0.10$ that is somewhat lower than the value estimated for the best-fitting in the uncorrected case. This however does not alter the main conclusion: IC 1459 can be successfully fitted without invoking dark matter. Note however, that the error bars for h_4 are rather large in the outer

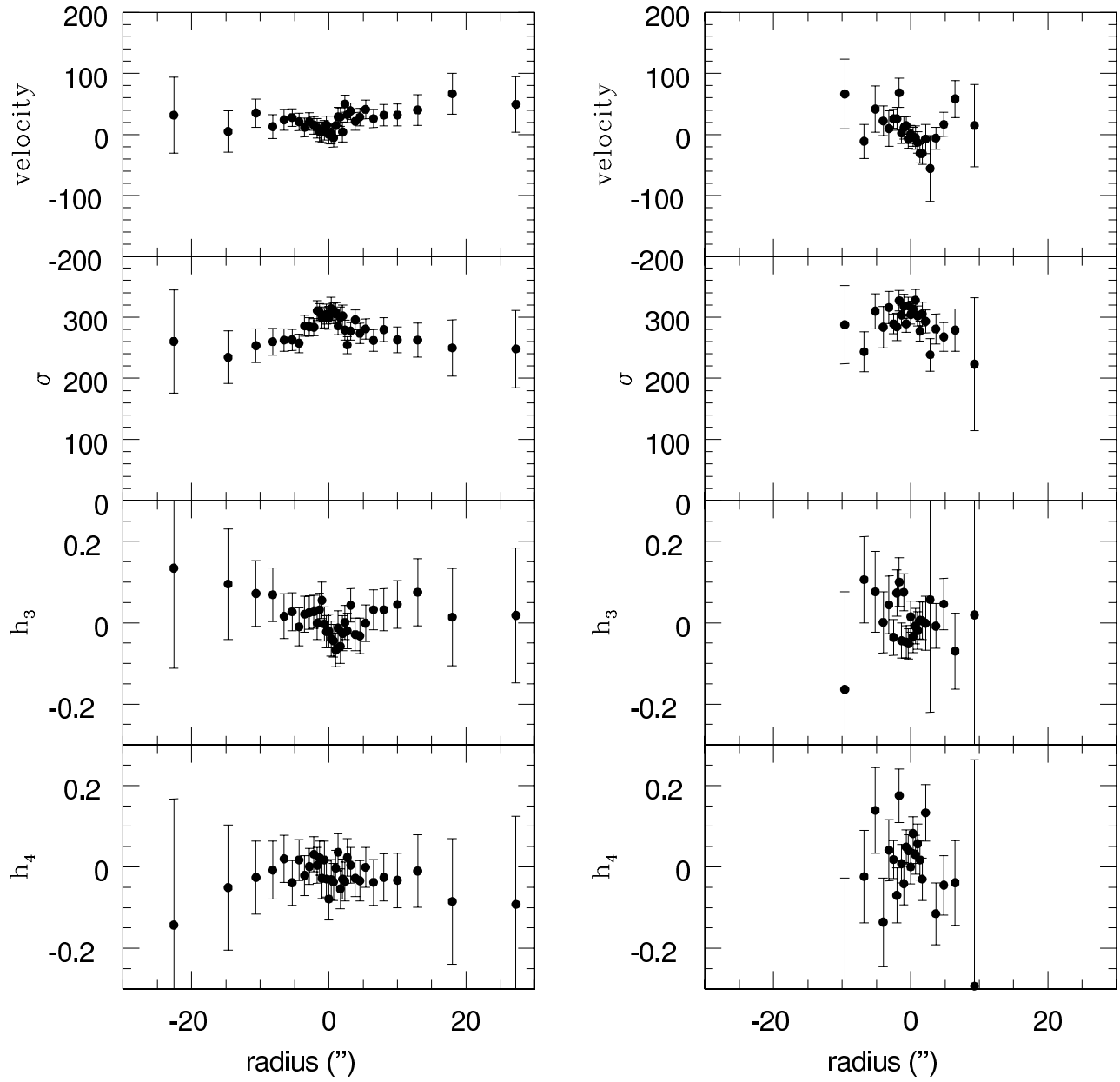


Figure 7. Stellar kinematics of NGC 4105 for major (left) and minor (right) axis. From top to bottom: velocity, velocity dispersion, h_3 and h_4 parameters.

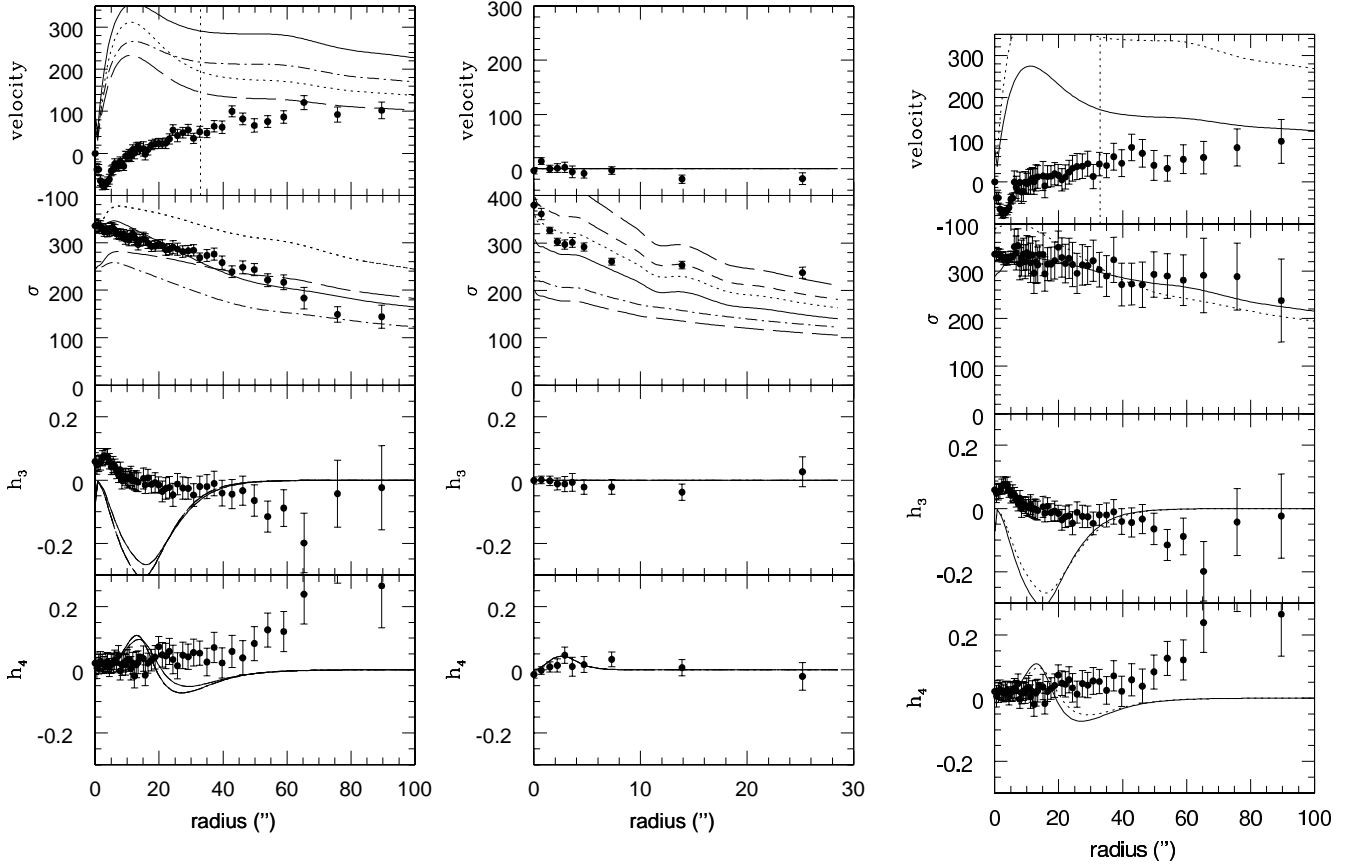


Figure 8. Predictions of the two-integral models for IC 1459. *Left:* major axis predictions. Solid lines: $k = 1$, $M/L_B = 6.83$, no dark matter included, no embedded disc. Dashed lines: $k = 0.6$, $M/L_B = 3.81$, no dark matter included, without embedded disc. Dotted lines: $k = 0.6$, $M/L_B = 6.83$, no dark matter included, without embedded disc. Dot-dashed lines: $k = 1$, $M/L_B = 3.81$, no dark matter included, without embedded disc. *Middle:* minor axis predictions. Dotted line: $k = 1$, $M/L_B = 8.54$, no dark matter included, without embedded disc. Dashed line: $k = 0.6$, $M/L_B = 3.05$, no dark matter included, without embedded disc. Solid line: $k = 0.6$, $M/L_B = 7.33$, no dark matter included, without embedded disc. Dot-dashed line: $k = 1$, $M/L_B = 3.05$, no dark matter included, without embedded disc. Thick long dashed line: $k = 1$, $M/L_B = 14.23$, no dark matter included, without embedded disc. Thick short dashed line: $k = 0.6$, $M/L_B = 12.21$, no dark matter included, without embedded disc. Vertical dotted line indicates one effective radius; in case of the minor axis it is out of scale. *Right:* Predictions of the two-integral models for the major axis of IC 1459 for *corrected* values of the observed velocity and velocity dispersion (see text for details). Dotted line: $k = 1$, $M/L_B = 9.56$, no dark matter included, no embedded disc. Solid line: $k = 0.6$, $M/L_B = 5.31$, no dark matter included, without embedded disc.

parts. New observations of IC 1459 made (but still unpublished) by Bridges et al. (2003) should hopefully clarify the mass at $\sim 3R_e$.

Minor axis (Fig. 8 (middle panel)): Three $k = 0.6$ cases are plotted: one for $M/L_B = 3.05$ (dashed line) which does not provide a good fit for the velocity dispersion, and the other one for which $M/L_B = 7.33$ that provides a better agreement (solid line). Finally, a thick short dashed line gives a prediction of the velocity dispersion for $M/L_B = 12.21$ and obviously does not provide a good fit (except marginally at ~ 30 arcsec). A better fit was obtained using $k = 1$: with the dotted lines we present a case with $M/L_B = 8.54$ (no dark matter, no embedded disc). However, a fit with $k = 1$, but with a lower value of mass-to-light ($M/L_B = 3.05$, dot-dashed line) predicts a velocity dispersion that is too low. Finally, if one increases mass-to-light ratio to $M/L_B = 14.23$ (thick long dashed line) one can get a prediction that seems valid at ~ 25 arcsec. Values of both velocity and h_3

parameter are consistent with zero for the minor axis, and h_4 is fitted properly for these cases.

We have shown that in the case of the major axis the best-fitting for the velocity dispersion can be obtained using $k = 1$ and $M/L_B = 6.83 \pm 0.13$ (or 5.31 ± 0.10 obtained using corrected values of v and σ). However, with these assumptions the velocity is enormously high. This means that one is faced with the same situation that BDI described in the case of NGC 720. Therefore, as in BDI, one can conclude that IC 1459 *cannot have* a distribution function of the form $f(E, L_z)$, and that three-integral modelling is needed.

The results for the minor axis modelling are inconclusive because the observations go out only to $\sim 1R_e$. The slight tendency for the velocity dispersion to flatten in the outer parts of the minor axis could be a result of a predominance of tangential orbits possibly suggested by the trend seen in the h_4 parameter.

Because of the counterrotating core there is a strong

hint that IC 1459 is the result of a merger. That is why we compared the results of Bendo & Barnes (2000) who used an N-body code to study the LOSVD of simulated merger remnants with the stellar kinematics that we extracted. A reasonable agreement is seen in fig. 9 by Bendo & Barnes (2000) which shows the dependence of the Gauss-Hermite parameters as functions of position along the major axis for a typical 3:1 merger (merger between disc galaxies with mass ratios of 3:1). Although in the central parts there is a small discrepancy between the observations and the simulation, in the outer parts there is an obvious trend for an increase in the h_4 parameter. A further detailed comparison is difficult to perform because we do not know how to scale exactly Bendo & Barnes simulation to our observed data because we do not know the effective radius of the simulated merger. In the case of IC 1459 we have no way of knowing what the mass ratio of two disc galaxies might have been as well as other parameters involved in the simulation (such as inclination angles of the merging galaxies). For the core region we find $v/\sigma \approx 0.29$. Note, that for a quoted Bendo & Barnes simulation this ratio is about one. This is only a rough comparison but we hope that future studies of the projected kinematics of simulated merger remnants will bring new insights to the problem of the formation of the counterrotating cores and the formation of early-type galaxies in general, as the number of observed kinematical profiles increases.

5.2 IC 3370

As might be expected the axisymmetric modelling of IC 3370 did not give a good fit to the observed data given the strong isophotal twisting present in this galaxy. We used the inclination angle of 50° that gave the best (but far from perfect) results. This inclination angle implies intrinsic axis ratio of ~ 0.7 . In Fig. 9 we present our modelling results for major, minor and intermediate axis.

Major axis (Fig. 9 (panel (a))): for the major axis $k = 0.6$ (dotted lines) gives a good fit in the inner regions (~ 25 arcsec) for the velocity. A good fit is obtained in the outer regions (> 50 arcsec) for the velocity dispersion. On the contrary, $k = 1$ provides a good fit for the velocity in the outer region ($> 1R_e$); the velocity dispersion seems to be fitted well throughout the whole galaxy with $k = 1$. We experimented with the inclusion of the inner embedded disc of 6 arcsec, but this does not change much the results. The decrease of the velocity dispersion follows very closely the constant mass-to-light prediction (out to $\sim 3R_e$). Both h_3 and h_4 are fitted reasonably in all the given cases. The mass-to-light ratio found in all the cases at $\sim 3R_e$ is ~ 5.4 . Since in this case, for the major axis, both the h_3 and h_4 parameters are consistent with zero we did not apply the correction of the velocity and velocity dispersion as we did in the case of IC 1459.

Minor axis (Fig. 9 (panel (b))): because of the fact that the axisymmetric modelling predicts zero velocity for the minor axis, a successful fit could not be achieved (the same is true for the h_3 parameter). Modelling of the velocity dispersion therefore provided a possibility for several interesting tests. One can see that a $k = 0.6$ fit (dotted line, $M/L_B = 4.80$, no dark matter, no embedded disc) cannot produce a successful fit for the velocity dispersion. Therefore, in all other tests in the case of the minor axis

we used $k = 1$. With the solid line we present the case of $M/L_B = 6.59$ without the embedded disc which provided a better, but still unsatisfactory fit to the data. Again, the inner embedded disc of 6 arcsec was included. Therefore, we increased the mass-to-light ratio to 9.68 (case without the dark matter and with the disc represented with the thick dashed line) to achieve a better agreement. Still better agreement is obtained when one increases further the mass-to-light ratio to 12.65: this is the case without the dark matter and the included disc represented by the thick dot-dashed line. Note, however, the discrepancy in the inner parts of the galaxy.

Intermediate axis (Fig. 9 (panels (c) and (d))): Several tests were done using lower values of the constant mass-to-light ratio: the modelling of the *uncorrected* values of the observed velocity and velocity dispersion are given in panel (c) and the modelling of the *corrected* points is given in panel (d). Successful fits for the velocity dispersion are obtained for $k = 1$ (again the $k = 0.6$ case can be ruled out). All the models with $k = 1$ give a good fit for the velocity in the inner parts of the galaxy (~ 20 arcsec) and they all fail in the outer parts. In a similar manner they all reproduce well the velocity dispersion profile. h_3 and h_4 parameters are fitted reasonably throughout the whole galaxy (modelled h_3 shows departures in the outer region and h_4 shows small departures from the data in the inner part). We note the improvement of the modelling when the points corrected for non-zero values of h_3 and h_4 are used (see Fig. 9, panel d).

Strictly speaking IC 3370 should not be modelled using the axisymmetric modelling technique. However, this technique permits the following conclusion. In IC 3370 up to $\sim 3R_e$ the dark matter halo is not needed for the successful modelling: the mass-to-light ratio varies between ~ 5 (based upon the major axis data) and ~ 13 (based upon the minor axis data). Note however, that $M/L_B \sim 13$ is the upper limit, because it must be stressed that this kind of modelling of the observed minor axis dispersions tends to *overestimate* the mass-to-light ratio (as given in BDI): this modelling, for a given M/L_B underestimates the minor axis dispersions since the model will be flattened by enhanced v_ϕ^2 which does not contribute to the minor axis profile. The real galaxy is flattened by enhanced v_z^2 which contributes on the minor axis.

5.3 NGC 3379

NGC 3379 is a galaxy for which the evidence for dark matter is scarce (Ciardullo et al. 1993, Romanowsky et al. 2003). We present our results for the two-integral axisymmetric modelling for the major and minor axis in Fig. 10. The inclination angle that we used in all the cases was 40° because it gave the best fit to the observed data.

Major axis (Fig. 10 (left)): When one takes $k = 1$ and does not include either a dark matter halo or an internal embedded disc, using $M/L_B = 5.44$ (dotted lines) one gets an exaggerated value of the velocity but a rather reasonable fit for the velocity dispersion (especially in the inner part). In all other cases for the major axis we will use $k = 0.5$ which provides a better fit to the data in the outer part of NGC 3379. Using a mass-to-light ratio, $M/L_B = 4.75$, without an embedded disc and without a dark halo combination

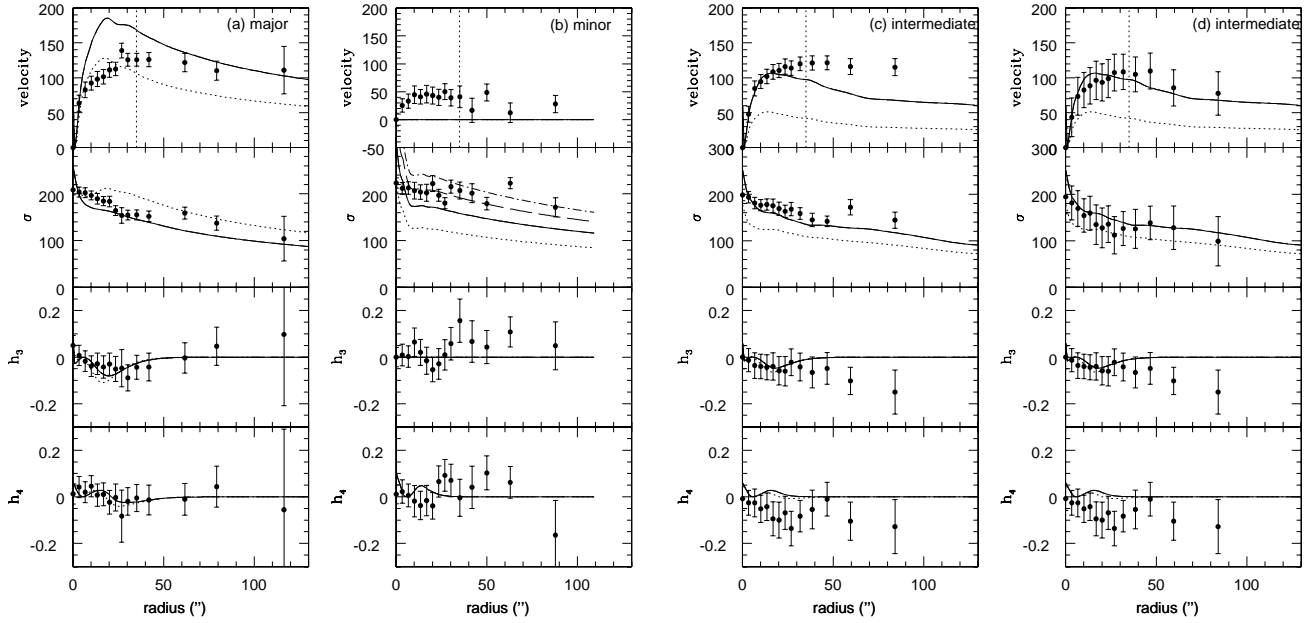


Figure 9. Predictions of the two-integral models for IC 3370. *Panel (a):* major axis predictions. Dotted lines: $k = 0.6$, $M/L_B = 5.42$, no dark matter included, no embedded disc. Solid lines: $k = 1$, $M/L_B = 5.28$, no dark matter included, no embedded disc. *Panel (b):* minor axis predictions. Dotted line: $k = 0.6$, $M/L_B = 4.80$, no dark matter included, no embedded disc. Solid line: $k = 1$, $M/L_B = 6.59$, no dark matter included, no embedded disc. Thick dashed line: $k = 1$, $M/L_B = 12.64$, no dark matter, embedded disc. Thick dot-dashed line: $k = 1$, $M/L_B = 9.68$, no dark matter, embedded disc. *Panel (c):* Intermediate axis predictions for the *uncorrected* values of the observed velocity and velocity dispersion. Dotted lines: $k = 0.6$, $M/L_B = 3.64$, no dark matter included, no embedded disc. Solid lines: $k = 1$, $M/L_B = 5.19$, no dark matter included, no embedded disc included. *Panel (d):* Intermediate axis predictions for the values corrected for non-zero values of h_3 and h_4 of the observed velocity and velocity dispersion. The meaning of the curves is the same as in plot (c). Vertical dotted line indicates one effective radius.

gives a good fit for the velocity dispersion in the outer regions. Also, a case with $M/L_B = 5.44$ (dashed line), without the embedded disc and without a dark halo gives a good fit in the outer part of the galaxy. Both h_3 and h_4 parameters are fitted similarly in all the models and the fit is very close to the observed values. Note that since the outermost points for the velocity dispersion and h_4 parameter appear to be discordant, we followed the advice of the referee and put a greatly increased error bar in order to provide a real uncertainty of these quantities. To get a better fit in the inner regions (interior to ~ 15 arcsec) we performed a test using low $k = 0.4$, inclination angle of 50° and $M/L_B = 4.58$: this is shown in Fig. 10 using a thick dot-dashed line.

Minor axis (Fig. 10 (right)): Because this galaxy does not show a strong rotation on the minor axis, the velocity was fitted properly in this approach which assumes axisymmetry. In the case of the minor axis we consider various tests related to the velocity dispersion. With a dotted line we present the $k = 1$ case with $M/L_B = 4.18$ without the dark matter, and without a disc: this does not provide a good fit. Neither can the case with $k = 0.5$ without a dark matter halo and a disc, with $M/L_B = 4.18$ which is represented with a dashed line. The thick dot-dashed line represents a case for which $M/L_B = 6.69$ ($k = 0.5$, without dark matter, and with embedded disc) and which provides a good fit in the inner region (out to $\sim 1R_e$), but fails in the outer regions. On the contrary, a test made with $M/L_B = 8.91$ and

$k = 0.5$ (thick long dashed line) provides a good fit in the outer regions (beyond $\sim 1R_e$).

Our conclusion based upon the two-integral modelling that we performed is that in NGC 3379 there is no evidence for dark matter out to $\sim 1.46R_e$ and that this galaxy can be fitted with a constant mass-to-light ratio that is between ~ 5 and ~ 9 . The minor axis modelling suggests a mass-to-light increasing with radius, while the major axis does not. This discrepancy could be due to the third-integral effects. These results are in agreement with the papers by other authors using entirely different techniques. Ciardullo et al. (1993) found that NGC 3379 does not possess a dark halo, and that mass-to-light ratio is ~ 7 (their observations of PNe extend out to ~ 200 arcsec). Also, they used distance of 10.1 Mpc to NGC 3379; if we apply the value of 13 Mpc used in our calculations the mass-to-light ratio in the B -band will become equal to 5.9 ± 0.9 . Romanowsky et al. (2003) obtained the value $M/L_B = 7.1 \pm 0.6$ at ~ 200 arcsec taking the distance of 10.3 Mpc; again if we apply the value of 13 Mpc used in our applications we calculate the mass-to-light ratio in the B -band of 5.8 ± 0.5 . Their results are similar to ours at smaller radius and taken together they fail to demonstrate the presence of DM over this range of radius.

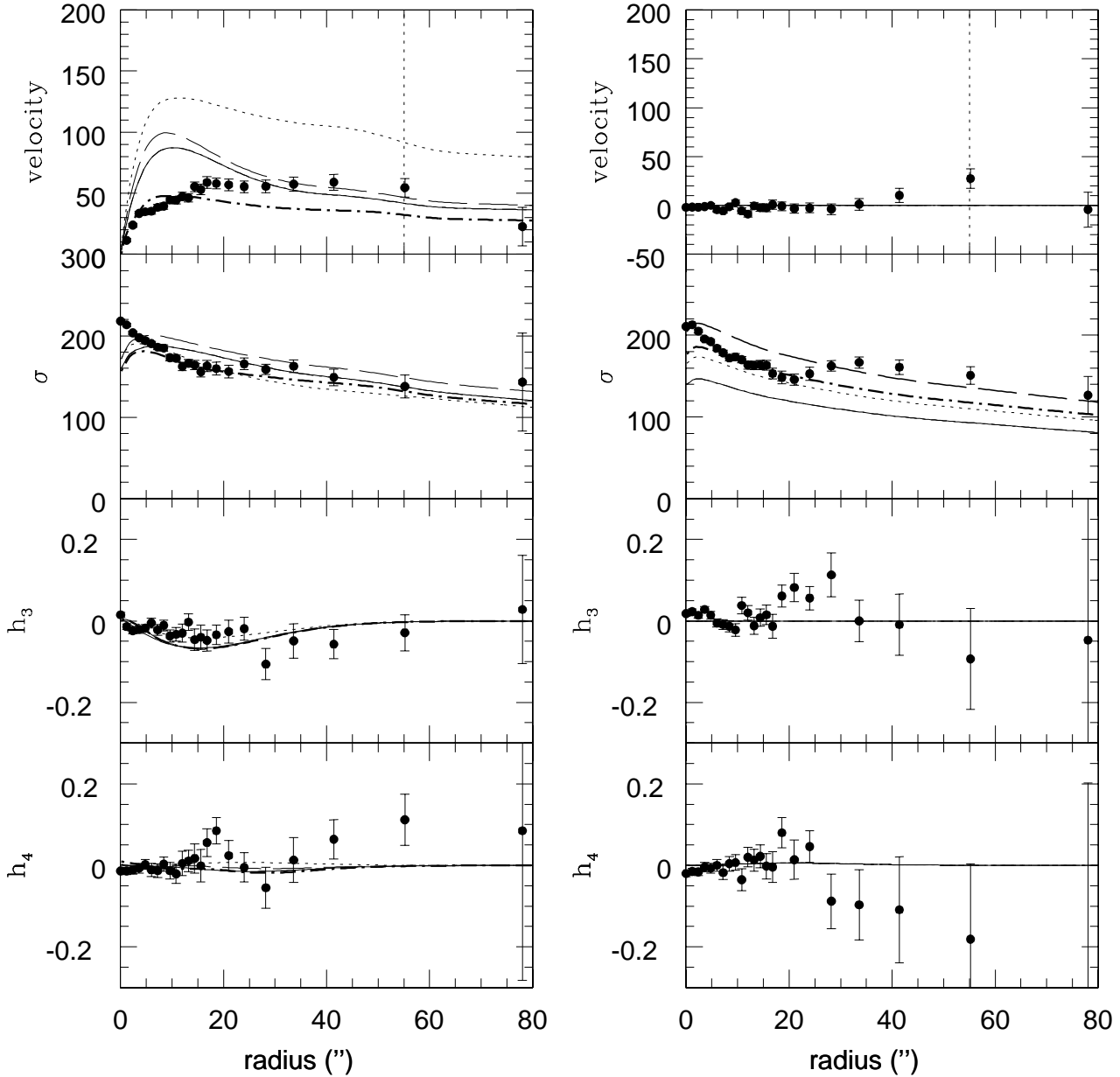


Figure 10. Predictions of the two-integral models for NGC 3379 compared to data. *Left:* major axis predictions. Dotted lines: $k = 1$, $M/L_B = 5.44$, no dark matter included, no embedded disc. Dashed lines: $k = 0.5$, $M/L_B = 5.44$, no dark matter included, without embedded disc. Solid lines: $k = 0.5$, $M/L_B = 4.75$, no dark matter included, embedded disc included. Thick dot-dashed line: $k = 0.4$, $M/L_B = 4.58$ no dark matter included, with embedded disc. *Right:* minor axis predictions. Dotted line: $k = 1$, $M/L_B = 4.18$, no dark matter included, without embedded disc. Solid line: $k = 0.5$, $M/L_B = 4.18$, no dark matter included, embedded disc included. Thick long dashed line: $k = 0.5$, $M/L_B = 8.91$, no dark matter included, without embedded disc. Thick dot-dashed line: $k = 0.5$, $M/L_B = 6.69$, no dark matter included, with embedded disc. Vertical dotted line indicates one effective radius.

5.4 NGC 4105

We present our results for the two-integral axisymmetric modelling for the major and minor axis in Fig. 11. The inclination angle that we used in all the cases was 50° because it gave the best fit to the observed data.

Major axis Fig. 11 (left): The case of $k = 0.5$ and $M/L_B = 4.50$ (no dark matter halo, no disc included) pro-

vided the best-fitting to the velocity dispersion for the distance > 2 arcsec (dotted line). However, this case (as well as all the others mentioned below) predicts a grossly excessive velocity. The solid lines show the predictions of the case with $k = 1$, $M/L_B = 4.50$ (no dark matter halo, disc included), for which the velocity is again exaggerated, and velocity dispersion is lower than observed (although beyond

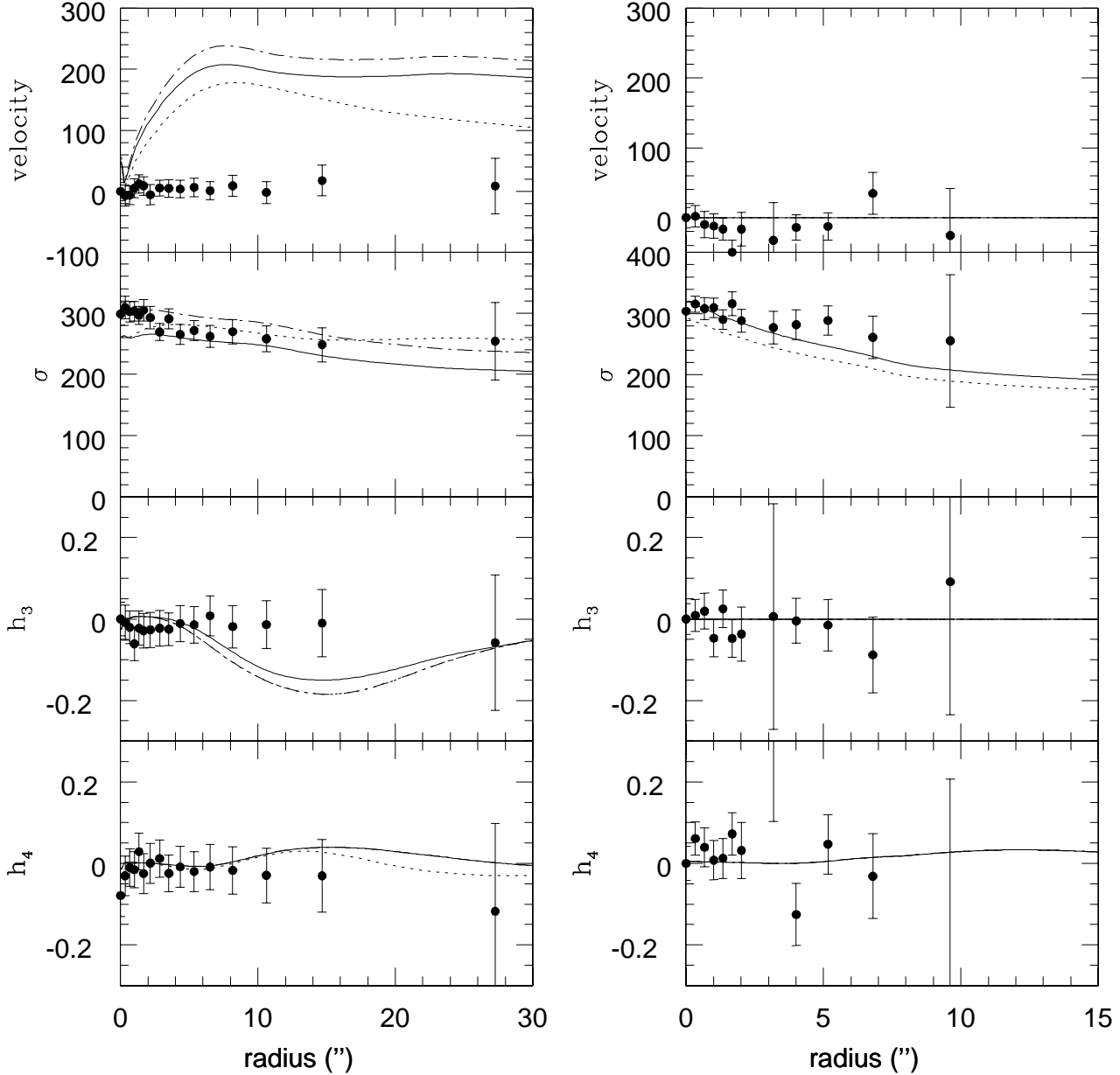


Figure 11. Predictions of the two-integral models for NGC4105 compared to data. *Left:* major axis predictions. Dotted lines: $k = 0.5$, $M/L_B = 4.50$, no dark matter included, with embedded disc. Solid lines: $k = 1.0$, $M/L_B = 4.50$, no dark matter included, embedded disc included. Dot-dashed lines: $k = 1$, $M/L_B = 5.94$, without dark matter, with embedded disc. *Right:* minor axis predictions. Dotted line: $k = 0.5$, $M/L_B = 5.86$, no dark matter included, without embedded disc. Dashed line: $k = 1$, $M/L_B = 6.42$, no dark matter included, without embedded disc (overlapped by solid line). Solid line: $k = 1$, $M/L_B = 6.42$, no dark matter included, embedded disc included. Dashed line: $k = 0.5$, $M/L_B = 5.86$, without dark matter, without embedded disc. Note the difference in scales for two different axes.

~ 2 arcsec within the error bars). We experimented with the embedded discs of 6 arcsec (radius inside which the P.A. changes): their inclusion did not change much the final results. Finally, with a dot-dashed line we present the case of $k = 1$, $M/L_B = 5.94$ (no dark matter halo, disc included), that predicts an even larger velocity, but a good fit to the velocity dispersion. The h_3 parameter predictions provide a rather good agreement with the observations (apart from

the region between 10 and 20 arcsec related to the large rotational velocity curve which is not seen in the data and is probably related to the problem of the existence of the second integral). The h_4 parameter is fitted properly in all the cases. A good fit for the velocity could not be obtained; various mass distributions could not solve the problem of the fit to this quantity.

Minor axis Fig. 11 (right)): The case of $k = 0.5$ and $M/L_B = 5.86$ (no dark matter halo, no disc included) did not provide a successful fit to the velocity dispersion for a radius < 10 arcsec (dotted line). The solid line is for the case of $k = 1$ and $M/L_B = 6.42$ (without dark matter, and without a disc) and this represents the best fit in all cases. Since h_3 and h_4 do not show large departures from zero, they are fitted properly.

Our conclusion for NGC 4105 is that this galaxy should be modelled using a three-integral approach because the rotation and velocity dispersion cannot be fitted simultaneously (the modelling results are very similar to these obtained in the case of IC 1459 above, and NGC 720 from BDI). However, judging by two-integral modelling one can see that the dark matter is not needed (out to $\sim 1 R_e$) and that a successful fit (only for dispersion, for reasons given above) can be obtained for a constant mass to light ratio $M/L_B \sim 6$.

5.5 Schwarzschild modelling

Because of numerous problems with fitting our 4 galaxies using 2I technique we have also performed several tests using the three-integral Schwarzschild (1979) orbit superposition modelling which included spherical, axisymmetric and triaxial potentials. Our procedures were based on the Rix et al. (1997) paper. We have implemented a method for extraction of the velocity profiles from the orbit libraries based on the so-called self-organizing maps (SOMs) (Kohonen 1997; Murtagh 1995) and the results obtained so far are only indicative: we found that the constant mass-to-light ratio potentials could provide satisfactory fits to the observed data, but more testing is needed. When performing the orbits superposition in the triaxial potential special attention must be given to selection of the representative orbit libraries. Our results so far did not differ much when we used the libraries which contained exclusively box or tube orbits. Nevertheless, it is difficult to justify *a priori* a given selection of orbits. Development of this methodology is proceeding.

6 X-RAY PROPERTIES OF IC 1459, NGC 3379 AND NGC 4105

Of the four galaxies presented in this paper, IC 1459, NGC 3379 and NGC 4105 are known to possess an X-ray halo.

X-rays are important for the early-type galaxies because they can provide independent constraints on the masses and mass-to-light ratios out to large radii (for a review see Danziger 1997; Mathews & Brighenti 2003). The basic assumptions and formulae are as follows. One assumes that spherical symmetry holds, and that the condition of hydrostatic equilibrium is valid:

$$\frac{dP_{\text{gas}}}{dr} = -\frac{GM(r)\rho_{\text{gas}}}{r^2}, \quad (12)$$

where $M(r)$ is the mass interior to the radius r , and the gas obeys the perfect gas law:

$$P_{\text{gas}} = \frac{\rho_{\text{gas}}kT_{\text{gas}}}{\mu m_H}, \quad (13)$$

where μ is the mean molecular weight for full ionization (taken to be 0.61), and m_H is the mass of the hydrogen atom. From these two equations one can give the expression for the gravitating mass interior to radius r :

$$M(r) = -\frac{kT_{\text{gas}}r}{G\mu m_p} \left(\frac{d \ln \rho}{d \ln r} + \frac{d \ln T_{\text{gas}}}{d \ln r} \right). \quad (14)$$

If one wants to calculate the mass and mass-to-light ratio of an elliptical galaxy based upon X-ray observations one can use the following approach (which was used in Kim & Fabbiano (1995), hereafter KF95, for NGC 507 & NGC 499): one assumes circular symmetry and derives a radial profile of the X-ray surface brightness measured in concentric rings centered on the X-ray centroid. In a given range one then fits the analytic King approximation model:

$$\Sigma_X \sim \left[1 + \left(\frac{r}{a} \right)^2 \right]^{-3\beta+0.5} \quad (15)$$

(for details see KF95). Here a is the core radius (the radius where the surface brightness falls to half of its central value), and slope β . If the temperature of the X-ray emitting gas does not change much as a function of radius one can assume isothermality; we assumed that this holds in all the cases below. Now, using this assumption, one can estimate the total gravitational mass at a given radius r (assuming hydrostatic equilibrium) in a convenient form (KF95):

$$M_T = 1.8 \times 10^{12} (3\beta + \alpha) \left(\frac{T}{1 \text{keV}} \right) \left(\frac{r}{10^3 \text{''}} \right) \left(\frac{d}{10 \text{Mpc}} \right) M_{\odot}, \quad (16)$$

here the exponent α is related to the temperature ($T \sim r^{-\alpha}$) and is taken to be zero, and $\beta = 0.5$ (for IC 1459 and NGC 4105) and $\beta = 0.64$ (for NGC 3379) (Brown & Bregman 2001). This formula is valid outside the core region.

The mass-to-light ratio (in the B-band) can be expressed as a function of radius r :

$$\frac{M_T}{L_B} = 1.16 \times 10^{-2} 10^{\frac{B}{2.5}} (3\beta + \alpha) \left(\frac{T}{1 \text{keV}} \right) \left(\frac{r}{10^3 \text{''}} \right) \left(\frac{d}{10 \text{Mpc}} \right)^{-1}, \quad (17)$$

where B is the B magnitude of galaxy inside radius r (Kim & Fabbiano 1995).

The temperature of the X-ray halo can be estimated using a simple formula which connects the stellar velocity dispersion, σ and the virial temperature (see Mathews & Brighenti 2003):

$$T_{\text{vir}} \approx \mu m_p \sigma^2 / k \sim 10^7 \text{ K} \sim 1 \text{ keV}, \quad (18)$$

where μ is the mean molecular weight. After insertion of the value for $\mu = 0.61$ this equation can be rewritten in a convenient form:

$$kT_{\sigma[\text{keV}]} = 6.367 \times 10^{-6} \sigma_{[\text{km/s}]}^2 \quad (19)$$

where the temperature is given in keV and the stellar velocity dispersion, σ , is given in km s^{-1} .

In Figs. 12, 13 and 14 we sum graphically the results of the 2I modelling of IC 1459, NGC 3379 and NGC 4105 and estimates based on the X-rays calculations (beyond one effective radius; this limit is taken because we want to avoid the problems due to cooling flows in the central region and because we are interested in the comparison of different methodologies in the outer regions of the galaxies where dark matter is expected to play a significant role). 2I modelling is represented with a stripe which roughly indicates

the uncertainty within which the kinematics of these galaxies can be fitted (see discussion on 2I modelling above). The range of values $M/L_B = 5 - 10$ encompasses the full range of plausible possibilities shown in Fig. 8.

In the case of IC 1459 (Fig. 12), the stripe related to the X-rays is determined using the paper by Davis & White (1996) who found $T = 0.60^{+0.12}_{-0.13}$. This is in agreement with Fabbiano et al. (2003) who estimated $T = 0.5-0.6$ keV. We have also added a line which corresponds to $T = 0.4$ keV and which provides the best fit to the 2I modelling. Using virial assumption (Eq. 19) one gets $T_\sigma = 0.73$ keV (see Fig. 16). Only in the case of $T = 0.50 - 0.60$ keV do we have a marginal agreement (in region $1.0 < r < 2R_e$) with results obtained using 2I modelling techniques.

This may mean that:

(i) the 2I integral models systematically underestimate the mass-to-light ratio. This is possible but not probable since the estimated values of the mass-to-light ratio (M/L_B was found to be between ~ 6 and ~ 10 , see the stripe in Fig. 12) are in a good agreement with the mean value found in the sample of van der Marel (1991) which after rescaling to the Hubble constant of $70 \text{ km s}^{-1} \text{ Mpc}^{-1}$ becomes $M/L_B = 8.33 \pm 0.35$. This type of modelling precludes the possibility that with an observed decreased velocity dispersion one could have a dark matter halo with a consequent increase of a mass-to-light ratio;

(ii) the temperature estimates used above are not correct – note, however, that if we adopt a lower temperature, e.g. $T \sim 0.5$ keV (still allowed by the measurements of Fabbiano et al. 2003 and Davis & White 1996) a better agreement can be obtained (dotted line in Fig. 12); the strong rising trend of the mass-to-light ratio will persist making this new estimate again larger in the outer part of the galaxy. Only $T \sim 0.4$ keV (as calculated in the paper by Brown & Bregman 1998) (dashed line in Fig. 12) would provide an agreement within the whole region (beyond $\sim 1R_e$) for which we have the 2I mass-to-light ratio estimate;

(iii) the assumption of the hydrostatic equilibrium for IC 1459 is not correct, so the usage of Eq. (12) is inappropriate which makes Eq. (17) inapplicable in this case. We will address the problem of the departures from the hydrostatic equilibrium in a forthcoming paper (Samurović & Danziger 2005, in preparation) and we here refer a reader to a very recent important work by Ciotti & Pellegrini (2004) which investigates the effects of deviations from equilibrium on the mass of ellipticals.

In Figures 13 and 14 we display graphically the results of the 2I modelling and estimates based on the X-rays calculations (beyond one effective radius) for the mass-to-light ratio in the B -band of NGC 3379 and NGC 4105. The X-ray estimate for the mass-to-light ratio in the B -band is again given as a shaded area with the lower limit given as T_σ and the upper limit $T_X = 1.5T_\sigma$, because Brown & Bregman (1998) for objects with few counts assumed this latter limit. For several galaxies Brown & Bregman (1998) found that $T_X \approx 2T_\sigma$: this relation as our choice was used only in the case of NGC 3379 thus giving an additional corresponding upper limit. The case for which $T_X = 1.5T_\sigma$ is also plotted as a thick dotted line in Fig. 13. We have chosen to look at the temperature as virial because of the weak signal from X-rays. In the case of NGC 3379 we plotted available results on the mass-to-light ratio that were obtained using

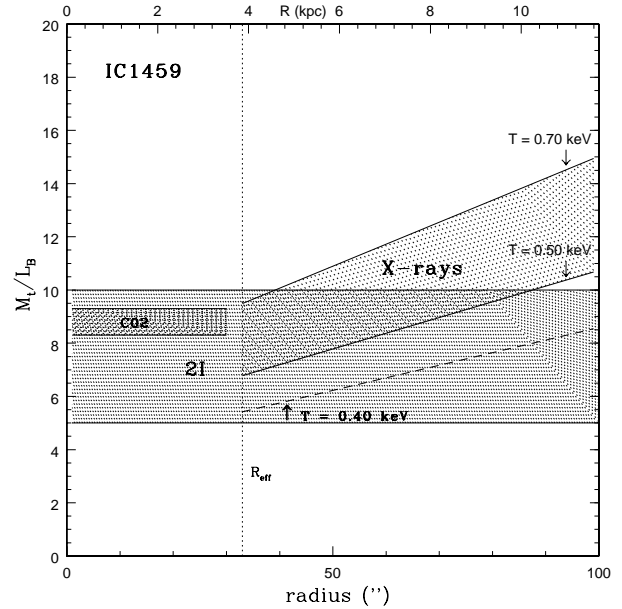


Figure 12. Cumulative mass-to-light ratio of IC 1459 in the B -band as a function of radius. The scale of the lower x-axis is given in arc seconds and the upper x-axis is in kiloparsecs. The effective radius is plotted as a dashed vertical line. Limits on the mass based on the X-rays are given using lower and upper limits obtained using Davis & White (1996): $T = 0.60 \pm 0.10$ keV. “2I” refers to two-integral modelling: the stripe in the 2I case provides the limits within which the kinematics can be fitted (see text for details). One additional line (see text for details) was also added to the plot: dashed line is for the case for which $T = 0.4$ keV. The stripe labelled with C02 corresponds to the estimate obtained by Cappellari et al. (2002) of the M/L ratio which is, after the conversion to the B -band and the distance used in our paper, $M/L_B = 8.8 \pm 0.5$.

PNe (Ciardullo et al. 1993 (C93), and Romanowsky et al. 2003 (R03)). Here we note a caveat that the X-ray and PN models are merely spherical.

Our conclusions regarding comparison of the results for the mass-to-light ratio obtained using 2I modelling techniques and X-ray approach are the following:

NGC 3379 (Fig. (13)): the estimates from 2I modelling are in an agreement with the X-ray estimates. Our M/L ratios are similar to those obtained for PNe albeit at larger radii. We note that beyond 120 arcsec ($\sim 2.2R_e$) a discrepancy between PNe estimates and X-ray estimate occurs. If we reduce the value of the β parameter from 0.64 to 0.5 we obtain a good agreement with the data between $\sim 1R_e$ and $\sim 1.5R_e$; between ~ 1.5 and $\sim 3.5R_e$ the mass-to-light ratio in the B -band varies between 5.5 and 9.5. In Fig. (13) we also plotted a point (at $1R_e$) and a stripe based on the paper by Gebhardt et al. (2000) which is calculated using their 3I modelling procedure.

NGC 4105 (Fig. (14)): since in the case of this galaxy our data extend only out to $\sim 1R_e$ the comparison of the X-ray predictions with the results of the 2I modelling interior to this point could not be done. It is however obvious that if one assumes that the constant mass-to-light ratio inferred from the 2I modelling is valid beyond $1R_e$ there is a clear discrepancy between the predictions of the two methodolo-

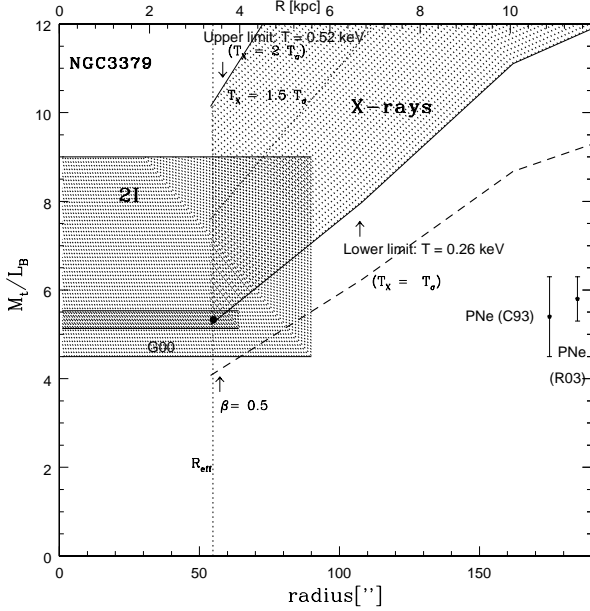


Figure 13. Cumulative mass-to-light ratio of NGC 3379 in the B -band as a function of radius. The meaning of the symbols is the same as in Fig. 12. Two additional points are given in the plot: R03 refers to Romanowsky et al. (2003), C93 to Ciardullo et al. (1993). Two upper limits are given: one for $T_X = 1.5T_*$ represented by a thick dotted line, and one for which $T_X = 2T_*$ as a solid line. The dashed line is for the case for which $T_X = 0.26$ keV and $\beta = 0.5$. The point labelled G00 and corresponding stripe are based on the result from the 3I modelling of Gebhardt et al. (2000); it has been obtained for the B -band and at the distance of 13 Mpc.

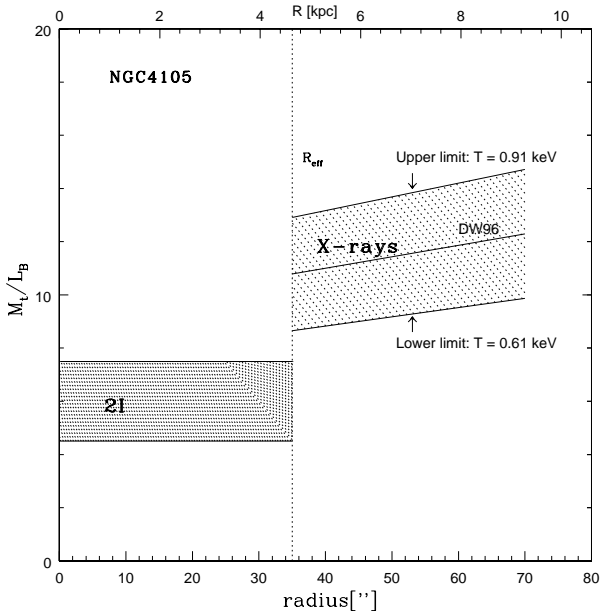


Figure 14. The same as in Fig. 13 but for NGC 4105. DW96 refers to the temperature taken from the paper by Davis & White (1996).

gies: the value of the mass-to-light ratio from the X-rays is higher (at $\sim 2R_e$ $M/L_B \sim 12$) than that obtained using the 2I modelling (assumed to be between ~ 5 and ~ 7). We did not have data related to other mass tracers, so further comparisons were not possible.

Using these findings, together with the recent result of Peng et al. (2004) who have recently found that for NGC 5128 at $15 R_e$ the mass-to-light ratio is only 13 (in the B -band), we can infer that for both NGC 3379 and NGC 5128 there is a discrepancy between the mass-to-light ratios calculated using X-rays and PNe techniques at the large radii (beyond $3R_e$) from the centre. For the sake of comparison of the X-ray and PNe we use the recent analysis of Kraft et al. (2003) who studied NGC 5128: using their X-ray data out to 15 kpc ($\sim 3R_e$) they found that the total mass $\sim 2 \times 10^{11} M_\odot$. This is in very good agreement with the value obtained using data, technique and assumptions by Peng et al. (2004) (for $\beta_* = 0$). At the larger distance ($\sim 15R_e$) using this approach the total cumulative mass becomes equal to $\sim 5 \times 10^{11} M_\odot$ (Peng et al. 2004).

Accepting now to a first order approximation that the X-ray results discussed above are realistic we solve the Jeans equation which provides the connection between the anisotropy and the temperature of the hot interstellar gas through which the stars move. First we write the Jeans equation for the radial stellar velocity dispersion σ_r (Binney & Tremaine 1987 Sec 4.2):

$$\frac{1}{\ell_*} \frac{d(\ell_* \sigma_r^2)}{dr} + \frac{2\beta_* \sigma_r^2}{r} = -\frac{GM(r)}{r^2} \quad (20)$$

where ℓ_* is the stellar luminosity density which corresponds to the radial (σ_r) and transverse (σ_θ) stellar velocity dispersions. Spherical symmetry is assumed and the equation is valid for a non-rotating system. By introducing a parameter β_* ⁴ one can express the nonspherical nature of the stellar velocity dispersion:

$$\beta_* = 1 - \frac{\overline{v_\theta^2}}{\sigma_r^2} \quad (21)$$

where $\overline{v_\theta^2} = \overline{v_\theta^2} + \sigma_\theta^2$. If $0 < \beta_* < 1$ the orbits are predominantly radial, which means that the line of sight velocity profile becomes more strongly peaked than a Gaussian profile (h_4 positive), and for $-\infty \leq \beta_* < 0$ the orbits are mostly tangential, which means that the profile is more flat-topped than a Gaussian (h_4 negative) (Gerhard 1993, van der Marel & Franx 1993). The β_* parameter can be determined from the observations: we used the estimates of the h_4 parameter to calculate β_* (as given in Gerhard 1993 and van der Marel & Franx 1993) in the case of IC 1459. In our study we use the estimates by Kronawitter et al. (2000) for NGC 3379 obtained using 2I modelling including h_4 fitting. For NGC 4105 we will assume that $\beta_* = 0$ (spherical isotropic case) given the small observed h_4 parameter consistent with zero throughout the galaxy (but, nevertheless, we will also test some anisotropic models). We solve the Jeans equation (20) using equation (16) to express the total mass of a given galaxy at the position r . For the stellar luminosity density we adopt the Hernquist (1990) profile:

⁴ Note that here we will use β_* instead of the usual β symbol to avoid confusion with the previously defined parameter which is related to the slope used in the analytic King approximation model (equation 16).

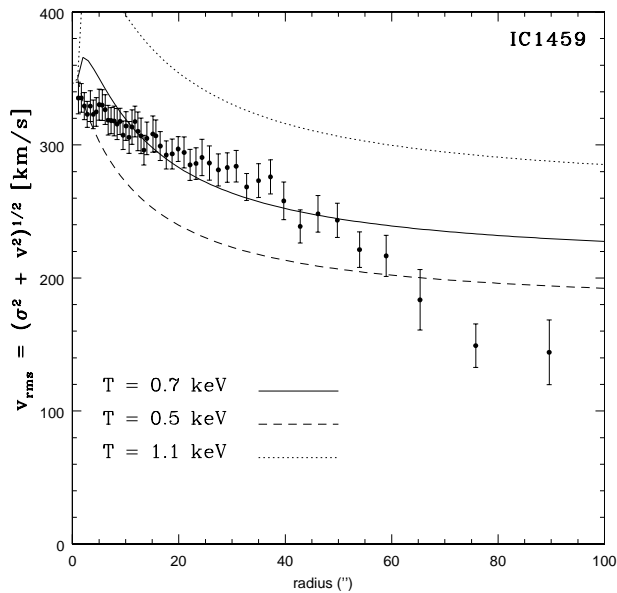


Figure 15. Dynamical modelling of the *uncorrected* velocity dispersion of IC 1459 using X-ray data. The modelling lines based on different masses which correspond to different temperatures are the following: the case of $T = 0.7$ keV is given with a solid line, the case of $T = 0.5$ keV is given with a dashed line and the case of $T = 1.1$ keV is given with a dotted line. In all cases spherical isotropy ($\beta_* = 0$) and hydrostatic equilibrium are assumed.

$$\ell_* = \frac{L}{2\pi} \frac{a}{r} \left(\frac{1}{r+a} \right)^3 \quad (22)$$

where $R_e = 1.8153a$. The projected line-of-sight velocity dispersion is calculated as (e.g. Binney & Mamon 1982; Mathews & Brighenti 2003):

$$\sigma^2(R) = \frac{\int_R^{r_t} \sigma_r^2(r) [1 - (R/r)^2 \beta_*] \ell_*(r) (r^2 - R^2)^{-1/2} r dr}{\int_R^{r_t} \ell_*(r) (r^2 - R^2)^{-1/2} r dr} \quad (23)$$

where the truncation radius, r_t , extends well beyond the last observed kinematical point. We took for NGC 3379 $r_t = 2R_e$, for NGC 4105 $r_t = 1.5R_e$ and for IC 1459 $r_t = 4R_e$. Solving equation (23) using a given value of T (known from X-ray observations, or calculated using stellar velocity dispersion) one can find the β_* parameter which provides the best agreement with the observed data (it is important to underline, in the case of the hydrostatic equilibrium).

As a check we tested the well known case of NGC 4472 studied by Mathews & Brighenti (2003). We confirm that indeed only with $\beta_* \sim 0.7$ can one obtain a good agreement with the observed velocity dispersion for this galaxy. As noted recently by Ciotti & Pellegrini (2004) this value of the β_* parameter is unrealistically high which may lead to the important conclusion that the assumed condition of the hydrostatic equilibrium is not valid.

Using the aforementioned approach we reached the following conclusions for the three early-type galaxies with the X-ray haloes given in this paper:

(i) IC 1459 (Fig. (15)). First, we tested a spherical isotropic model ($\beta_* = 0$) using different estimates for the temperature: $T = 0.7$ keV (solid line), $T = 0.5$ keV (dashed

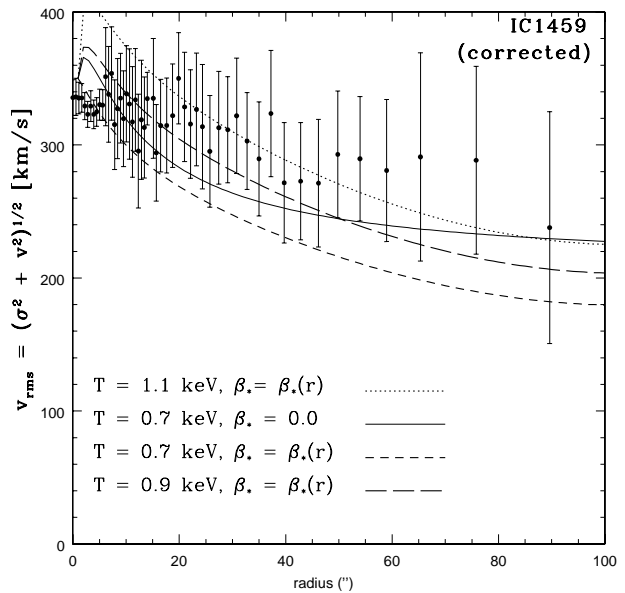


Figure 16. Dynamical modelling of the velocity dispersion corrected for non-zero values of the h_4 parameter of IC 1459 using X-ray data. The modelling lines based on different masses which correspond to different temperatures are the following: the case of $T = 0.7$ keV is again given with a solid line ($\beta_* = 0$) and a short dashed line is for the case of $T = 0.7$ keV ($\beta_* = \beta_*(r)$). The case of $T = 0.9$ keV and $\beta_* = \beta_*(r)$ is given with a long dashed line and the case of $T = 1.1$ keV and $\beta_* = \beta_*(r)$ is given with a dotted line. Again, in all cases hydrostatic equilibrium is assumed.

line) and $T = 1.1$ keV (dotted line). In all three cases spherical isotropy ($\beta_* = 0$) and validity of hydrostatic equilibrium were assumed and the values of the velocity dispersion were uncorrected (in the sense of Eq. 11). Only the case for which $T = 0.7$ keV can provide a good fit to the observed data out to ~ 50 arcsec. In the outer regions the *observed* velocity dispersion tends to decrease and none of the fits is successful. This best-fitting value of $T = 0.7$ keV is, as expected, in an excellent agreement with the value found using a virial assumption (see Eq. 19). This value, however, is somewhat higher than our preferred value of $T = 0.4 - 0.6$ keV found with the 2I modelling, thus implying a higher X-ray based mass-to-light ratio than one inferred from stellar dynamics (as shown in Fig. 12).

Second, since for IC 1459 (Fig. 16) we have departures from zero of the h_4 which imply that radial orbits dominate ($h_4 > 0$ beyond ~ 20 arcsec) we have also modelled the corrected (again, in the sense of Eq. 11) values of the velocity dispersion: the measured points are the same as in Fig. 8 (right panel). The fit which uses $T = 0.7$ keV and $\beta_* = 0$ (the same as in Fig. 15 repeated here again with solid line) can produce a reasonable agreement with the data. If we now allow anisotropies ($\beta_* = \beta(r)$) based on our observed $h_4(r)$ values as given above we can see that $T = 0.7$ keV, except for the central parts (interior to ~ 20 arcsec) this fit given with the short dashed line fails to fit the corrected velocity dispersion. We assume that $h_4 \sim 0$ ($\beta_* \sim 0$) in the inner regions of the galaxy and in the outer parts at $\sim 3R_e$ h_4 is ~ 0.2 ($\beta \sim 1$). A slightly higher value of the temperature

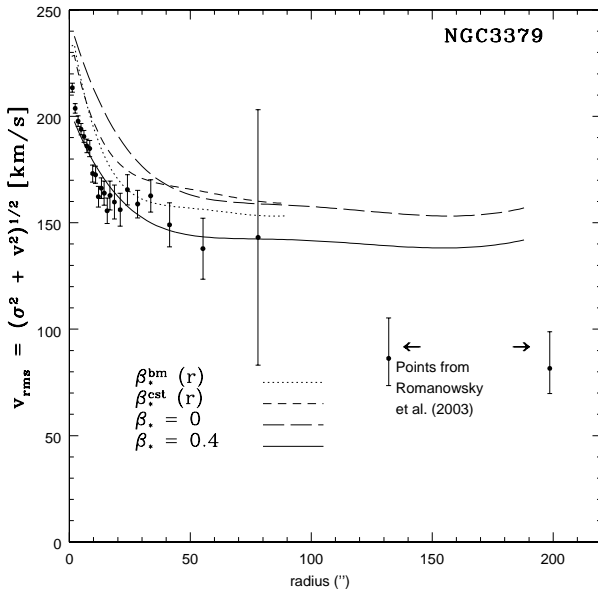


Figure 17. Dynamical modelling of the velocity dispersion of NGC 3379 using X-ray data. Observational points are folded about y -axis and are taken from Statler & Smecker-Hane (1999). Long dashed line is the spherical isotropic case ($\beta_* = 0$), when hydrostatic equilibrium is assumed. Thin solid line is for the case when hydrostatic equilibrium is assumed for which radial orbits dominate ($\beta_* = 0.4$). The short dashed line is based on the estimate of the β_* -parameter obtained for the constant mass-to-light ratio model (“cst” model) of Kronawitter et al. (2000) and the dotted line is based on the estimate of the β_* -parameter obtained for the “best model” (“bm”) of Kronawitter et al. (2000): they extend only interior to ~ 100 arcsec. Two outermost points given as filled circles are taken from Romanowsky et al. (2003).

of $T = 0.9$ KeV, taken together with the same anisotropies ($\beta_* = \beta(r)$) provides a better fit especially in the intermediate region (between ~ 10 and ~ 50 arcsec). Finally, a fit which used $T = 1.1$ KeV and $\beta_* = \beta(r)$ provides the best fit (among the ones tested) in the region between ~ 20 and ~ 100 arcsec. Again, in the case of the modelling of the corrected velocity dispersion data the value of the temperature based on the X-rays is higher than that inferred from stellar dynamics ($T \sim 0.4 - 0.5$ keV): the preferred value of $T = 1.1$ keV is higher than that in the uncorrected case ($T = 0.7$ keV). The reason for this discrepancy could be due to the inherent assumptions of the two methodologies (such as the validity of hydrostatic equilibrium and constant value of the temperature in the case of the X-rays and mass profile used in the case of the BDI approach; see also the discussion about the mass-to-light ratio of IC 1459 earlier in this Section). It is important to stress that before we can use the X-ray temperatures to model the velocity dispersion we need to understand the reasons for the differences which might be due to different types of mass profiles and/or problems with the BDI models.

(ii) NGC 3379 (Fig. (17)). In our modelling we have used the temperature $T = 0.26$ keV, as given in Table 1. A spherical isotropic model ($\beta_* = 0$) is excluded: in this case the model is completely inconsistent with the observed data. Two models based on the paper by Kronawitter et al. (2000)

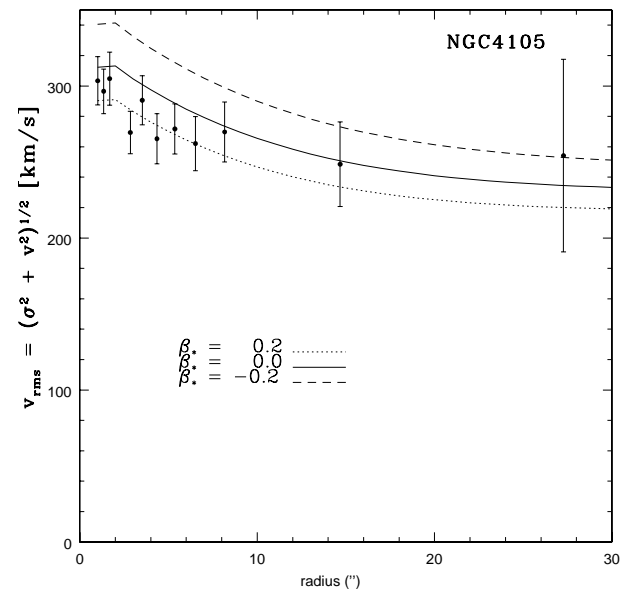


Figure 18. Dynamical modelling of the velocity dispersion NGC 4105 using X-ray data. Solid line is for the spherical isotropic case ($\beta_* = 0$), the dashed line is for the case of $\beta_* = -0.2$ (predominantly tangential orbits) and the dotted line is for the case of $\beta_* = 0.2$ (predominantly radial orbits).

do not provide a good fit to the data either: the case of the “best model” (dark matter implied: $0 < \beta_* < 0.3$) provides marginally better fit than that of the constant M/L ratio ($0 < \beta_* < 0.2$). After a failure to obtain a successful fit using β_* values taken from the literature we experimented with different (positive and constant) values of β_* : the case of $\beta_* = 0.4$ provides a very good fit to the data. Thus we can conclude that using the approach based on the X-rays (two-integral approach) we can say that for NGC 3379 the dark matter is not dynamically dominant to $\sim 1.5R_e$ because at $\sim 1.5R_e$ one can get the same cumulative mass-to-light ratio as it is obtained using stellar dynamical modelling. Note that the gradient of the mass seen in the X-rays is not consistent with the constant mass-to-light ratio. However, as in Mathews & Brighenti (2003) the value of the β parameter is larger than that obtained using stellar dynamics although not much. Note that in our 2I dynamical modelling we have used the h_4 parameter to describe the anisotropies and not β_* . We find that the positive value of the β_* parameter ($\beta \sim 0.4$) is in agreement with the positive values of the h_4 parameters ($h_4 \sim 0.05$) extracted from the observations and indicating radial anisotropies in the outer parts of NGC 3379 (for the relations between h_4 and β see van der Marel & Franx 1993, Gerhard 1993).

(iii) NGC 4105 (Fig. 18). In the modelling which we performed we have used the temperature $T = 0.76$ keV, as given in Table 1. A spherical isotropic model ($\beta_* = 0$) provides a good fit to the observed data (note that we again neglected possible influence of NGC 4106). We have also tested a case with $\beta_* = 0.2$ (predominantly radial orbits) which provides a reasonable fit to the observed velocity dispersion and a case with ($\beta_* = -0.2$) (predominantly tangential orbits) which does not provide a good fit to the data. Note that in the case

of NGC 4105 the error bars for the temperature of the X-ray halo given by Davis & White (1996) are huge (especially the upper one): $T_X = 0.76_{-0.69}^{+4.40}$ keV. However, as can be seen in Fig. 14 the value $T_X = 0.76$ keV falls just in the middle between the upper and lower limit as obtained from the stellar velocity dispersion which justifies its usage in the dynamical modelling which we performed. As a side note, we stress that with the upper limit of $T_X = 0.76 + 4.40 = 5.16$ keV no fit could be obtained to the velocity dispersion even in the case when the maximum allowed value of $\beta_* = 1$ was used: velocity dispersion values were always grossly exaggerated: $\sigma > 450$ km s⁻¹ throughout the whole galaxy.

7 DISCUSSION AND CONCLUSIONS

We presented the long-slit spectra of four early-type galaxies (IC 1459, IC 3370, NGC 3379 and NGC 4105) that extend out to $\sim 1 - 3R_e$ for which we extracted full LOSVDs. For NGC 3379 we had the observations out to $\sim 0.55R_e$ so for the modelling purposes we have used the data from the literature. The presented photometry of these four galaxies was necessary for the dynamical modelling which we performed. In this paper we have made two-integral (2I) modelling of these four galaxies and compared the results with the those obtained using the spherical X-ray modelling (in the case of IC 1459, NGC 3379 and NGC 4105).

(i) IC 1459 has a counter-rotating stellar core and its h_4 has in the outer parts values that are significantly different from zero implying the existence of radial anisotropies. We could not obtain the simultaneous fit to the velocity and velocity dispersion (for the major axis) which means that we are faced with a situation where the 2I approach is not completely satisfactory and that the motion of stars in this galaxy requires three integrals. However, study of the 2I modelling of the velocity dispersion permits us to draw conclusions about the constant mass-to-light ratio in this galaxy: we infer that in the B -band it is $5 < M/L_B < 10$ (in solar units, for the Hubble constant of 70 km s⁻¹Mpc⁻¹). Because of the fact that the velocity dispersion shows a decreasing trend compatible with a given constant mass-to-light ratio we conclude that up to $\sim 3R_e$ (~ 100 arcsec ≈ 11.7 kpc) there is no need for the dark matter halo, or at least, the contribution of the dark matter within this radius is dynamically unimportant. Of course, we cannot exclude the existence of the dark halo that is significant at the larger radii and we hope that the ongoing studies (which use globular clusters as mass tracers) will clarify this. Using the X-ray modelling we found that the temperatures of $T \sim 0.7$ keV (obtained in the uncorrected case) and $T = 1.1$ keV (obtained in the corrected case) can provide a good fit to the dynamics of IC 1459 interior to ~ 50 arcsec and between ~ 20 and ~ 100 arcsec respectively. This is higher than the value obtained using the stellar dynamics 2I modelling which lies between 0.4 and 0.6 keV. The difference between the BDI and Jeans approaches may be due to the fact that both approaches provide a different *prediction* of the X-ray temperature irrespective of the observed temperature (T_X) and irrespective of the validity of hydrostatic equilibrium: in this case the difference could be attributed to the different types of mass profiles used, and/or to the problems of the BDI modelling.

(ii) IC 3370 may be even a more complex galaxy to model with the 2I approach. This galaxy shows a large isophotal twist and it has a significant non-zero velocity on the minor axis which strongly suggests its triaxiality. Therefore, although 2I modelling necessarily provides a poor fit for some quantities (for example, velocity and h_3 parameter for the minor axis) it nevertheless can give some insight into the dark matter content based on the study of the velocity dispersion. Again, as in the case of IC 1459 we can conclude that the dark matter within $\sim 3R_e$ (~ 100 arcsec ≈ 20.3 kpc) is not needed (or it is not dynamically important) because we can obtain a good fit to the velocity dispersion using a constant mass-to-light ratio: $5 < M/L_B < 13$ (in solar units, for the Hubble constant of 70 km s⁻¹Mpc⁻¹). In the case of this galaxy an X-ray halo was not detected, so we did not perform the X-ray modelling.

(iii) For NGC 3379 based on the 2I modelling procedures we find no evidence for dark matter which dominates inside $\sim 1.5R_e$ and found that the constant mass-to-light ratio of this galaxy in the B -band for $h_0 = 0.7$ is between 5 and 9. This result is in agreement with previous studies of this galaxy (Ciardullo et al. 1993; Romanowsky et al. 2003). Analysis based on the X-rays leads to the same conclusion concerning the dark matter within $2R_e$ and the mass-to-light ratio of this galaxy if we adopt the parameters which are in agreement with those found in the literature: $\beta = 0.64$ (where β is the slope used in the analytic King approximation model) and the temperature of the X-ray halo is between ~ 0.26 ($=1T_\sigma$) and 0.52 ($=2T_\sigma$) keV where T_σ is the temperature based on the stellar velocity dispersion. (If we use $T_X = 0.25$ keV and $\beta = 0.5$, we can get a fit between ~ 1 and $\sim 1.5 R_e$ and between ~ 1.5 and $\sim 3.5R_e$ the mass-to-light ratio in the B -band varies between 5.5 and 9.5.) Solving Jeans equation we find that a spherical isotropic model ($\beta_* = 0$) is excluded. The observations of the stellar velocity dispersion (interior to $\sim 1.5R_e$) favour $\beta_* = 0.4$ (predominantly radial orbits) under the assumption of the hydrostatic equilibrium. Therefore, based on an X-ray analysis we conclude that interior to $\sim 1.5R_e$ the cumulative mass-to-light ratio is in agreement with that based on the dynamical modelling and therefore dark matter in NGC 3379 is not dynamically dominant in this region, although we note that the gradient of the mass profile is not consistent with the results from stellar dynamical modelling. Beyond $\sim 2R_e$ we note the discrepancies regarding the mass-to-light ratio based on the X-rays and that based on the PNe.

Therefore, regarding NGC 3379, we conclude that, until better estimates for both stellar velocity dispersions and the h_4 parameter are available, it remains difficult to reconcile predictions of the X-ray methodology with the observations of the stellar velocity dispersions at radii $> 2R_e$, without rather strong radial anisotropies for which strong hints are already available. The problems related to the X-ray methodology such as assumptions of hydrostatic equilibrium and the absolute value of the temperature T_X and its radial dependence together with the difficulties in X-ray binary source subtraction may also play their part in this complex situation.

(iv) NGC 4105: based on the 2I modelling procedures which we performed we find no evidence for dark matter inside $\sim 1R_e$ and found that the constant mass-to-light ratio of this galaxy in the B -band for $h_0 = 0.7$ is ~ 6 .

Since in the case of this galaxy we had observational data only out to $\sim 1R_e$ we did not do the comparison with the X-rays out to this radius. If we assume that the constant mass-to-light ratio of 5–7 (obtained using stellar dynamics) beyond $1R_e$ is still valid we notice a discrepancy between this value and X-ray predictions which give at $2R_e$ the value of ~ 12 . Since we did not have other tracers for the mass we could not make further comparisons as we did in the case of NGC 3379. Solving the Jeans equation we find that a spherical isotropic model ($\beta_* = 0$) in this case provides a good fit for a stellar velocity dispersion out to $\sim 1R_e$, although we cannot exclude a case for which $\beta_* \sim 0.2$. Dark matter out to $\sim 1R_e$ in both of these cases is not needed. We note that in our modelling (both 2I and X-ray) we neglected possible interaction with the companion galaxy NGC 4106.

To summarize, based on the dynamical modelling we could not unambiguously detect the significant amounts of dark matter in our four galaxies out to $\sim 1 - 3R_e$ within the uncertainty of the modelling. In the case of IC 1459, NGC 3379 and NGC 4105 we had an additional independent way to determine a mass-to-light ratio. We used the measurements of the temperature of their X-ray haloes and found that for IC 1459 there exists a discrepancy between the temperatures based on the 2I modelling ($T \sim 0.4 - 0.6$ keV) and that based on the X-ray modelling ($T \sim 0.7 - 1.1$ keV). For NGC 3379 the agreement between different methodologies is good: in its case between ~ 1 and $\sim 1.5R_e$ stellar dynamical modelling and X-ray modelling are in agreement. Unfortunately, for IC 3370 an X-ray halo was not detected so such an independent study was not possible. For IC 1459 and NGC 3379 beyond $\sim 3R_e$ and for NGC 4105 beyond $\sim 1R_e$ X-rays show the need for dark matter, but in these regions we may face orbit anisotropies (for example, radial, as hinted by positive values of the h_4 parameter in the cases of IC 1459 and NGC 3379). These anisotropies together with the inherent problems of the X-ray methodology (such as the assumption of spherical symmetry and lack of hydrostatic equilibrium) make the complex problem of dark matter in the early-type galaxies even more difficult. This is currently under investigation.

ACKNOWLEDGEMENTS

We thank K. Freeman and M. Carollo for providing the observational material for NGC 3379 and NGC 4105 presented in this work. We thank Francesca Matteucci for useful discussions and Piercarlo Bonifacio for the help with the MIDAS system. We thank Olivier Hainaut for providing the photometry of IC 3370. We acknowledge the use of the Gauss-Hermite Fourier Fitting Software developed by R.P. van der Marel and M. Franx and the use of the Two-integral Jeans modelling Software developed by R.P. van der Marel and J.J. Binney. This research has made use of the NASA/IPAC Extragalactic Database (NED) which is operated by the Jet Propulsion Laboratory, California Institute of Technology, under contract with the National Aeronautics and Space Administration. One of the authors (SS) has been partially supported by the Ministry of Science and Environmental Protection of the Republic of Serbia through the projects: no. 1468, “Structure Kinematics, and Dynamics of the Milky Way” and P1196 “Astrophysical Spectroscopy of

Extragalactic Objects”. S.S. was supported with grants from MIUR COFIN 1998 Prot. No. 9802909231-001, the “Regione Friuli-Venezia-Giulia” L.R. 3/98, CNAA Prot. No. 14/a and ASI Prot. No. I/R/043/02. S.S. expresses his gratitude to the TRIL (Training and Research in Italian Laboratories) programme of the Abdus Salam International Centre for Theoretical Physics. All unpublished observational material was obtained at ESO, La Silla and Mt. Stromlo and Siding Springs Observatory. We thank the referee, A. Romanowsky, for providing helpful comments.

REFERENCES

- Bendo G.J., Barnes J.E., 2000, MNRAS, 316, 315
 Binney J.J., 2004, in Ryder S., Pisano D.J., Walker M., Freeman K., eds., ASP Conf. Ser. Vol. 220, Dark Matter in Galaxies, p.3
 Binney J.J., Mamon, 1982, MNRAS, 200, 361
 Binney J.J., Merrifield M.R., 1998, Galactic Astronomy, Princeton Univ. Press, Princeton, NJ
 Binney J.J., Tremaine S., 1987, Galactic Dynamics, Princeton Univ. Press, Princeton, NJ
 Binney J.J., Davies R.D., Illingworth G.D., 1990, ApJ, 361, 78 (BDI)
 Bridges T. et al., 2003, in press, in Bridges T., Forbes D., eds, IAU General Assembly, July 2003, Joint Discussion 6: Extragalactic Globular Clusters and their Host Galaxies, preprint (astro-ph/0310324)
 Brown, B.A., Bregman J.N., 1998, ApJ, 495, L75
 Brown B.A., Bregman J.N.: 2001, ApJ, 547, 154
 Capaccioli M., Held E.V., Lorenz H., Vietri M., 1990, AJ, 99, 1813
 Cappellari M., Verolme, E.K., van der Marel, R.P., Kleijn, G. A. Verdoes, Illingworth, G.D., Franx, M., Carollo, C.M., de Zeeuw, P.T., 2002, ApJ, 578, 787
 Carollo C.M., Danziger I.J., Buson L., 1993, MNRAS, 265, 553
 Carollo C.M., de Zeeuw P.T., van der Marel R.P., Danziger I.J., Qian E.E., 1995, ApJ, 441, L25
 Ciardullo R., Jacoby G.H., Dejonghe H.G., 1993, ApJ, 414, 454
 Cinzano P., van der Marel, R.P., 1994, MNRAS, 270, 325
 Ciotti L., Pellegrini S., 2004, MNRAS, 350, 609.
 Côté P., McLaughlin D.E., Cohen J.G., Blakeslee J.P., 2003, 591, 850
 Cretton N., van der Bosch F.C., 1999, ApJ, 514, 704
 Cretton N., Rix H-W., de Zeeuw P.T., 2000, ApJ, 536, 319
 Danziger I.J., 1997, in Persic M., Salucci P., eds., ASP Conf. Ser. Vol. 117, Dark and Visible Matter in Galaxies, p. 28
 Davis D.S., White R.E., 1996, ApJ, 470, L35
 De Bruyne V., Dejonghe H., Pizzella A., Bernardi M., Zeilinger W.W., 2001, ApJ, 546, 903
 De Rijcke S., Dejonghe H., Zeilinger W.W., Hau G.K.T., 2003, A& A, 400, 119
 Fabbiano G. et al., 2003, ApJ, 588, 175
 Fasano G., Bonoli C., 1989, A& ASS, 79, 291
 Fisher D., 1997, AJ, 113, 950
 Forbes D.A., Reizel D.B., Williger G.M., 1995, AJ, 109, 1576
 Gebhardt K. et al., 2000, AJ, 119, 1157

- Gerhard O., 1993, MNRAS, 265, 213
 Gerhard O., Jeske G., Saglia R.P., Bender R., 1998, MNRAS, 295, 197
 Gregg, M.D., Ferguson, H.C., Minniti, D., Tanvir, N., Catchpole, R., 2004, AJ, 127, 1441
 Hernquist L., 1990, ApJ, 356, 359
 Jaffe W., 1983, MNRAS, 202, 995
 Jarvis B., 1987, AJ, 94, 30 (J87)
 Kim D.-W., Fabbiano G., 1995, ApJ, 441, 182 (KF95)
 Kohonen T., 1997, Self-Organizing Maps, Springer-Verlag, Berlin and Heidelberg
 Kraft R.P., Vázquez S.E., Forman W.R., Jones C., Murray S.S., Hardcastle M.J., Worrall D.M., Churazov E., 2003, ApJ, 592, 129
 Kronawitter A, Saglia R.P., Gerhard O., Bender R., 2000, A& AS, 144, 53
 Loewenstein M., White R.E., 1999, ApJ, 518, 50
 Longhetti M., Rampazzo R., Bressan A., Chiosi C., 1998, A& AS, 130, 267
 Mathews W.G., Brighenti F., 2003, ARA& A, 41, 191
 Méndez, R.H., Riffeser, A., Kudritzki, R.-P., Matthias, M., Freeman, K.C., Arnaboldi, M., Capaccioli, M., Gerhard, O. E., 2001, ApJ, 563, 135
 Murtagh F., 1995, Pattern Recognition Letters, 16, 399
 Peng E.W., Ford H.C., Freeman K.C., 2004, ApJ, 602, 685
 Reduzzi L., Rampazzo R., 1996, A & AS, 116, 515
 Richtler T. et al., 2004, AJ, 127, 2094
 Rix H.-W., de Zeeuw P.T., Cretton N., van der Marel R.P., Carollo C.M., 1997, ApJ, 488, 702
 Romanowsky A.J., Douglas N.G., Arnaboldi M., Kuijken K., Merrifield M.R., Napolitano N.R., Capaccioli M. & Freeman K.C., 2003, Sci, 5640, 1696
 Saglia R.P. et al., 1993, ApJ, 403, 567
 Saglia R.P., Kronawitter A., Gerhard O. & Bender R., 2000, AJ, 119, 153
 Samurović S., Ćirković M.M., Milošević-Zdjelar V., 1999, MNRAS, 309, 63
 Sargent W.L.W., Schechter P.L., Boksenberg A., Shortridge K., 1977, AJ, 212, 326
 Schwarzschild M., 1979, ApJ, 232, 236
 Simkin S.M., 1974, A& A, 31, 129
 Slee O. B., Sadler E. M., Reynolds J. E., Ekers R.D., 1994, MNRAS, 269, 928
 Sparks W. B., Hough J.H., Axon D.J., Bailey J., 1986, MNRAS, 218, 429
 Statler T.S., 1995, AJ, 109, 1371
 Statler T., 2001, ApJ, 121, 244
 Statler T., Smecker-Hane T., Cecil G., 1996, AJ, 111, 1512
 Statler T., Dejonghe H., Smecker-Hane T., 1999, ApJ, 117, 126
 Statler T., Smecker-Hane T., 1999, ApJ, 117, 839
 Statler T., McNamara, B.R., 2002, ApJ, 581, 1032
 Tonry J.L., 1983, ApJ, 266, 58
 Tonry J., Davis M., 1979, AJ, 84, 1511
 van der Marel R.P., 1991, MNRAS, 253, 710
 van der Marel R.P., Franx M., 1993, ApJ, 407, 525
 van der Marel R.P., Binney J.J., Davies R.L., 1990, MNRAS, 245, 582
 Verdoes Kleijn G. A., van der Marel R. P., Carollo C. M., de Zeeuw P.T., 2000, AJ, 120, 1221
 Williams T.B., Schwarzschild M., 1979, ApJ, 227, 56

Table 1. Photometric data of IC 1459

Radius	B_{maj}	B_{min}
1.12	17.54	17.53
2.24	17.69	17.57
3.36	17.98	17.93
4.48	18.26	18.31
5.60	18.53	18.64
6.72	18.75	18.94
7.84	18.97	19.23
8.96	19.17	19.44
10.08	19.35	19.65
11.20	19.52	19.84
12.32	19.63	20.01
13.44	19.77	20.13
14.56	19.87	20.27
15.68	19.97	20.41
16.80	20.07	20.54
17.92	20.18	20.62
19.04	20.26	20.77
20.16	20.33	20.82
21.28	20.38	20.94
22.40	20.51	21.01
23.52	20.60	21.13
24.64	20.72	21.20
25.76	20.78	21.28
26.88	20.85	21.35
28.00	20.93	21.41
29.12	20.99	21.48
30.24	21.06	21.55
31.36	21.09	21.56
32.48	21.14	21.69
33.60	21.26	21.79
34.72	21.29	21.81
35.84	21.32	21.81
36.96	21.36	21.92
38.08	21.45	22.01
39.20	21.46	22.05
40.32	21.54	22.07
41.44	21.57	22.15
42.56	21.68	22.23
43.68	21.68	22.26
44.80	21.71	22.28
45.92	21.79	22.38
47.04	21.83	22.48
48.16	21.84	22.54
49.28	21.91	22.56
50.40	21.99	22.66
51.52	22.07	22.71
52.64	22.06	22.78
53.76	22.10	22.84
54.88	22.13	22.82
56.00	22.25	22.83
57.12	22.26	22.95
58.24	22.32	22.98
59.36	22.38	22.99
60.48	22.40	23.13
61.60	22.39	23.06
62.72	22.45	23.08
63.84	22.53	23.33
64.96	22.51	23.22
66.08	22.56	23.27
67.20	22.63	23.28
68.32	22.65	23.16
69.44	22.64	23.45
70.56	22.76	23.62

Table 2. Photometric data of IC 1459 (cont.)

Radius	B_{maj}	B_{min}
71.68	22.77	23.57
72.80	22.79	23.51
73.92	22.82	23.53
75.04	22.81	23.68
76.16	22.98	23.62
77.28	22.89	23.60
78.40	23.04	23.74
79.52	23.03	23.88
80.64	23.00	23.87
81.76	23.15	23.92
82.88	23.07	24.58
84.00	23.17	24.18
85.12	23.00	24.17
86.24	23.25	24.54
87.36	23.21	24.24
88.48	23.16	24.21
89.60	23.34	24.72
90.72	23.34	24.38
91.84	23.34	24.04
92.96	23.34	23.59
94.08	23.36	23.82
95.20	23.32	24.70
96.32	23.44	24.38
97.44	23.56	24.62
98.56	23.48	24.51
99.68	23.60	24.77

Table 3. Photometric data of IC 1459

Radius	ell	e_ell	a_4	e_ a_4	PA	e_PA
2.37	0.0789	0.0222	0.0098	0.0112	25.0340	8.5371
2.61	0.1555	0.0155	0.0014	0.0081	25.0340	3.1138
2.87	0.2305	0.0116	-0.0010	0.0064	29.3903	1.6299
3.16	0.2619	0.0070	-0.0036	0.0043	36.6932	0.9039
3.48	0.2469	0.0050	0.0048	0.0030	36.2416	0.6791
3.82	0.2217	0.0024	0.0040	0.0012	34.3339	0.3531
4.21	0.2208	0.0022	0.0048	0.0009	33.9219	0.3290
4.63	0.2181	0.0018	0.0043	0.0008	33.9717	0.2642
5.09	0.2207	0.0018	0.0041	0.0008	34.7649	0.2591
5.60	0.2239	0.0019	0.0043	0.0007	34.2680	0.2707
6.16	0.2237	0.0019	0.0045	0.0009	34.1239	0.2799
6.78	0.2259	0.0021	0.0073	0.0008	34.4263	0.3025
7.45	0.2295	0.0020	0.0080	0.0009	34.9283	0.2867
8.20	0.2357	0.0015	0.0065	0.0006	34.5964	0.2107
9.02	0.2385	0.0016	0.0077	0.0006	34.4031	0.2149
9.92	0.2416	0.0016	0.0062	0.0008	34.8394	0.2195
10.91	0.2413	0.0014	0.0062	0.0007	35.0805	0.1927
12.00	0.2481	0.0017	0.0068	0.0009	35.4974	0.2205
13.20	0.2576	0.0016	0.0081	0.0008	35.7242	0.2098
14.52	0.2631	0.0015	0.0054	0.0008	36.2231	0.1831
15.98	0.2670	0.0014	0.0043	0.0009	36.3186	0.1769
17.58	0.2721	0.0015	0.0015	0.0010	36.9959	0.1890
19.33	0.2781	0.0016	0.0055	0.0010	37.4972	0.1963
21.27	0.2816	0.0020	0.0037	0.0013	37.9748	0.2338
23.39	0.2743	0.0015	0.0009	0.0010	38.7111	0.1853
25.73	0.2669	0.0015	0.0036	0.0010	39.2994	0.1859
28.31	0.2743	0.0019	0.0031	0.0013	40.3620	0.2370
31.14	0.2746	0.0016	0.0072	0.0010	40.2397	0.1912
34.25	0.2735	0.0017	0.0062	0.0011	40.5417	0.2108
37.67	0.2799	0.0017	0.0037	0.0011	40.6800	0.2014
41.44	0.2793	0.0019	0.0025	0.0013	41.5781	0.2319
45.59	0.2734	0.0019	-0.0060	0.0012	41.6269	0.2277
50.14	0.2605	0.0021	0.0044	0.0013	42.3462	0.2649
55.16	0.2633	0.0017	-0.0022	0.0011	42.8055	0.2126
60.67	0.2633	0.0036	-0.0046	0.0032	42.8055	0.4574
66.74	0.3460	0.0166	0.0246	0.0128	42.8055	1.6807
73.42	0.2916	0.0121	0.0232	0.0085	44.9324	1.3949
80.76	0.2655	0.0040	0.0021	0.0027	42.7246	0.5053
88.83	0.2655	0.0039	-0.0096	0.0026	42.7246	0.4818
97.72	0.2866	0.0028	-0.0042	0.0020	43.5526	0.3290

Table 4. Photometric data of IC 3370

Radius	B_{maj}	B_{min}	ell	e_ell	a_4	e_ a_4	PA	e_PA
1.01	20.32	20.35	0.1779	0.0345	0.0023	0.0083	28.4463	6.3102
1.11	20.33	20.37	0.1532	0.0270	-0.0077	0.0051	30.3158	5.6492
1.22	20.35	20.39	0.1532	0.0272	-0.0076	0.0047	35.2232	5.5920
1.34	20.36	20.42	0.1671	0.0252	-0.0150	0.0116	35.5865	4.8310
1.47	20.38	20.44	0.1868	0.0315	-0.0204	0.0144	35.2309	5.3989
1.62	20.40	20.47	0.1999	0.0180	-0.0103	0.0087	34.9541	3.0065
1.78	20.43	20.50	0.2081	0.0180	-0.0136	0.0094	33.7971	2.8176
1.96	20.45	20.53	0.2071	0.0145	-0.0127	0.0072	34.3572	2.3044
2.16	20.48	20.56	0.2176	0.0107	-0.0070	0.0052	31.5482	1.6367
2.37	20.51	20.60	0.2250	0.0088	-0.0015	0.0034	30.4501	1.3044
2.61	20.54	20.65	0.2346	0.0095	-0.0002	0.0046	28.8893	1.3446
2.87	20.57	20.69	0.2461	0.0096	-0.0027	0.0047	28.1640	1.2951
3.16	20.61	20.74	0.2523	0.0087	-0.0076	0.0038	28.5882	1.1625
3.48	20.65	20.80	0.2578	0.0086	-0.0042	0.0040	28.2886	1.1202
3.82	20.70	20.85	0.2666	0.0089	0.0015	0.0036	28.5728	1.1267
4.21	20.75	20.92	0.2803	0.0080	0.0050	0.0034	28.5190	0.9652
4.63	20.80	20.99	0.3009	0.0089	0.0075	0.0040	28.6105	1.0058
5.09	20.86	21.06	0.3293	0.0104	0.0135	0.0056	28.0826	1.0915
5.60	20.93	21.14	0.3748	0.0127	0.0216	0.0068	27.5783	1.2197
6.16	21.00	21.23	0.4074	0.0115	0.0050	0.0069	27.2899	1.0344
6.78	21.07	21.33	0.4178	0.0099	-0.0096	0.0068	27.2899	0.8805
7.45	21.15	21.43	0.4241	0.0106	-0.0203	0.0073	24.5118	0.9281
8.20	21.24	21.54	0.3938	0.0146	-0.0264	0.0081	21.2977	1.3407
9.02	21.34	21.65	0.3673	0.0151	-0.0222	0.0082	19.2960	1.4664
9.92	21.44	21.78	0.3194	0.0107	0.0023	0.0050	20.5110	1.1535
10.91	21.55	21.91	0.2797	0.0113	0.0231	0.0060	19.6155	1.3511
12.00	21.66	22.04	0.2586	0.0079	0.0204	0.0047	22.4270	1.0151
13.20	21.79	22.19	0.2597	0.0054	0.0071	0.0034	26.4154	0.6823
14.53	21.92	22.34	0.2534	0.0049	0.0074	0.0032	29.5984	0.6348
15.98	22.06	22.50	0.2539	0.0057	0.0022	0.0037	32.0069	0.7313
17.58	22.21	22.66	0.2313	0.0055	0.0119	0.0035	32.3434	0.7686
19.33	22.37	22.83	0.2261	0.0059	0.0096	0.0036	32.9040	0.8371
21.27	22.53	23.01	0.2176	0.0073	0.0195	0.0045	33.7490	1.0765
23.39	22.70	23.18	0.2003	0.0063	0.0106	0.0038	32.9594	1.0006
25.73	22.88	23.36	0.1740	0.0063	0.0014	0.0038	37.2009	1.1426
28.30	23.06	23.53	0.1634	0.0073	-0.0059	0.0043	35.9724	1.3946
31.14	23.24	23.71	0.1631	0.0066	-0.0140	0.0039	36.6420	1.2666
34.25	23.43	23.88	0.1507	0.0088	-0.0254	0.0053	39.0821	1.8091
37.67	23.61	24.05	0.1439	0.0093	-0.0346	0.0056	38.3693	2.0001
41.44	23.80	24.21	0.1629	0.0070	-0.0267	0.0043	41.7802	1.3302
45.59	23.98	24.37	0.1481	0.0129	-0.0351	0.0090	48.1979	2.6974
50.14	24.16	24.53	0.2027	0.0100	-0.0275	0.0066	48.1979	1.5722
55.16	24.33	24.69	0.1798	0.0109	-0.0502	0.0080	48.8121	1.9028
60.67	24.49	24.86	0.1956	0.0102	-0.0325	0.0069	49.0052	1.6644
66.74	24.65	25.05	0.1956	0.0122	-0.0237	0.0078	47.0718	1.9807
73.42	24.80	25.25	0.1591	0.0144	-0.0433	0.0103	47.0718	2.8120
80.76	24.96	25.48	0.2944	0.0167	0.0311	0.0117	62.2400	1.9216
88.83	25.11	25.74	0.2116	0.0324	0.0656	0.0260	63.7530	4.7387
97.72	25.28	26.01	0.1937	0.0285	0.0158	0.0166	70.8523	4.2561

Table 5. Photometric data of NGC 3379

Radius	ell	e_ell	a_4	e_{a_4}	PA	e_PA
1.04	0.0420	0.0179	-0.0199	0.0077	31.7308	12.6662
1.15	0.0411	0.0144	-0.0182	0.0061	31.4050	10.1941
1.26	0.0364	0.0109	-0.0120	0.0048	30.9507	8.8246
1.39	0.0364	0.0090	-0.0100	0.0040	38.9286	7.2954
1.52	0.0468	0.0061	-0.0033	0.0029	38.9286	3.8845
1.68	0.0560	0.0065	-0.0033	0.0033	35.8077	3.4417
1.84	0.0497	0.0045	-0.0047	0.0021	35.2196	2.6751
2.03	0.0477	0.0040	0.0006	0.0019	42.1754	2.4513
2.23	0.0513	0.0029	-0.0018	0.0012	48.6264	1.6554
2.45	0.0484	0.0032	-0.0009	0.0015	46.5158	1.9447
2.70	0.0472	0.0024	0.0003	0.0011	49.1606	1.5022
2.97	0.0545	0.0020	0.0009	0.0010	52.3800	1.0774
3.27	0.0570	0.0016	0.0014	0.0007	53.0786	0.8062
3.59	0.0598	0.0018	0.0009	0.0009	58.6417	0.8868
3.95	0.0601	0.0014	0.0004	0.0006	59.2378	0.6864
4.35	0.0638	0.0016	0.0005	0.0008	61.9261	0.7383
4.78	0.0712	0.0012	0.0003	0.0006	64.9966	0.5020
5.26	0.0707	0.0013	0.0012	0.0007	66.1964	0.5561
5.79	0.0757	0.0013	-0.0000	0.0006	69.1280	0.5120
6.37	0.0801	0.0011	-0.0006	0.0005	69.6258	0.4070
7.00	0.0829	0.0009	0.0004	0.0005	70.0371	0.3291
7.70	0.0851	0.0009	0.0010	0.0005	71.3429	0.3188
8.47	0.0857	0.0009	0.0004	0.0005	71.5087	0.3147
9.32	0.0857	0.0008	0.0020	0.0004	72.4738	0.2620
10.25	0.0842	0.0007	0.0000	0.0004	73.0124	0.2546
11.28	0.0846	0.0007	0.0005	0.0004	73.2315	0.2527
12.41	0.0809	0.0008	0.0002	0.0004	73.2120	0.2892
13.65	0.0794	0.0008	0.0005	0.0004	73.5209	0.2851
15.01	0.0789	0.0008	-0.0001	0.0004	73.1663	0.2998
16.51	0.0809	0.0007	-0.0015	0.0004	73.6499	0.2755
18.16	0.0825	0.0008	-0.0011	0.0004	73.2797	0.2816
19.98	0.0823	0.0008	-0.0003	0.0004	73.3162	0.2944
21.98	0.0844	0.0008	-0.0008	0.0004	73.6756	0.2757
24.18	0.0842	0.0008	-0.0009	0.0004	73.1237	0.2663
26.59	0.0851	0.0008	-0.0010	0.0004	72.7601	0.2656
29.25	0.0837	0.0008	-0.0014	0.0005	72.6128	0.3025
32.18	0.0867	0.0010	-0.0006	0.0005	72.6128	0.3348
35.40	0.0909	0.0008	-0.0016	0.0005	72.5209	0.2780
38.94	0.0984	0.0019	-0.0017	0.0010	72.1395	0.5751
42.83	0.1018	0.0011	-0.0004	0.0006	72.3862	0.3325
47.11	0.1018	0.0038	0.0171	0.0047	72.3862	1.1097
51.82	0.1497	0.0050	0.0222	0.0028	72.3862	1.0235
57.01	0.1314	0.0024	-0.0002	0.0014	71.0137	0.5648
62.71	0.1296	0.0017	-0.0007	0.0009	69.7442	0.3917
68.98	0.1335	0.0017	0.0023	0.0009	69.7442	0.3833
75.88	0.1282	0.0021	-0.0016	0.0012	69.8391	0.5120
83.46	0.1352	0.0020	0.0002	0.0011	68.4398	0.4645

Table 6. Photometric data of NGC 4105

Radius	B_{maj}	B_{min}
1.01	16.60	16.44
1.34	16.79	16.68
1.68	16.99	16.95
2.02	17.17	17.19
2.35	17.34	17.40
2.69	17.48	17.57
3.02	17.58	17.75
3.36	17.70	17.90
3.70	17.78	18.02
4.03	17.90	18.13
4.37	17.97	18.25
4.70	18.09	18.38
5.04	18.17	18.45
5.38	18.25	18.53
5.71	18.36	18.63
6.05	18.41	18.74
6.38	18.51	18.82
6.72	18.57	18.87
7.06	18.66	18.94
7.39	18.71	19.05
7.73	18.76	19.09
8.06	18.83	19.14
8.40	18.90	19.27
8.74	18.97	19.27
9.07	19.00	19.31
9.41	19.04	19.39
9.74	19.09	19.48
10.08	19.13	19.45
10.42	19.19	19.48
10.75	19.24	19.61
11.09	19.29	19.57
11.42	19.38	19.76
11.76	19.37	19.69
12.10	19.41	19.80
12.43	19.44	19.76
12.77	19.55	19.86
13.10	19.52	19.94
13.44	19.51	19.91
13.78	19.57	19.93
14.11	19.67	19.99
14.45	19.70	20.02
14.78	19.64	19.97
15.12	19.67	20.05
15.46	19.67	20.12
15.79	19.74	20.12
16.13	19.83	20.10
16.46	19.82	20.15
16.80	19.91	20.18
17.14	19.90	20.24
17.47	19.85	20.23
17.81	19.91	20.22
18.14	19.97	20.37
18.48	19.93	20.26
18.82	20.03	20.33
19.15	19.93	20.36
19.49	19.90	20.33
19.82	20.03	20.39
20.16	19.98	20.30
20.50	20.10	20.43
20.83	20.14	20.44

Table 7. Photometric data of NGC 4105 (cont.)

Radius	B_{maj}	B_{min}
21.17	20.03	20.40
21.50	20.06	20.41
21.84	20.19	20.45
22.18	20.20	20.51
22.51	20.17	20.41
22.85	20.18	20.51
23.18	20.26	20.48
23.52	20.15	20.47
23.86	20.28	20.64
24.19	20.24	20.56
24.53	20.18	20.73
24.86	20.23	20.51
25.20	20.25	20.67
25.54	20.40	20.53
25.87	20.38	20.55
26.21	20.33	20.67
26.54	20.39	20.70
26.88	20.49	20.59
27.22	20.44	20.58
27.55	20.32	20.68
27.89	20.38	20.68
28.22	20.45	20.71
28.56	20.43	20.74
28.90	20.47	20.75
29.23	20.58	20.81
29.57	20.52	20.76
29.90	20.58	21.03

Table 8. Photometric data of NGC 4105

Radius	ell	e_ell	a_4	e_{a_4}	PA	e_PA
1.07	0.0309	0.0073	-0.0008	0.0029	198.5218	6.9764
1.18	0.0390	0.0064	-0.0034	0.0024	187.2130	4.8666
1.30	0.0461	0.0049	-0.0030	0.0016	179.1972	3.1360
1.42	0.0606	0.0037	-0.0022	0.0014	174.7109	1.7980
1.57	0.0718	0.0046	-0.0003	0.0017	169.7080	1.9388
1.72	0.0908	0.0034	0.0024	0.0014	164.3650	1.1180
1.90	0.1077	0.0031	0.0026	0.0015	160.6236	0.8842
2.09	0.1286	0.0041	0.0025	0.0021	157.5560	0.9839
2.29	0.1464	0.0037	0.0004	0.0021	156.5570	0.7885
2.52	0.1585	0.0033	-0.0042	0.0017	155.4411	0.6422
2.78	0.1635	0.0038	-0.0069	0.0015	154.9087	0.7275
3.05	0.1719	0.0055	-0.0097	0.0024	154.0606	1.0044
3.36	0.1802	0.0049	-0.0114	0.0022	151.7974	0.8679
3.70	0.1935	0.0045	-0.0098	0.0019	150.6190	0.7382
4.07	0.1966	0.0049	-0.0082	0.0024	151.6672	0.7954
4.47	0.2071	0.0043	-0.0048	0.0020	151.8860	0.6633
4.92	0.2068	0.0042	-0.0054	0.0018	152.9017	0.6469
5.41	0.2089	0.0044	-0.0055	0.0019	154.2281	0.6783
5.95	0.2071	0.0036	-0.0073	0.0018	153.8673	0.5592
6.55	0.2053	0.0033	-0.0042	0.0017	154.6262	0.5140
7.20	0.2149	0.0036	-0.0022	0.0017	153.3746	0.5293
7.92	0.2160	0.0033	-0.0038	0.0018	153.4159	0.4974
8.71	0.2126	0.0029	-0.0047	0.0017	153.2645	0.4434
9.59	0.2139	0.0032	-0.0067	0.0018	153.3385	0.4807
10.55	0.2095	0.0028	-0.0052	0.0017	153.6522	0.4293
11.60	0.2113	0.0031	-0.0044	0.0018	152.5015	0.4725
12.76	0.2143	0.0029	-0.0020	0.0018	153.5367	0.4342
14.04	0.2217	0.0030	-0.0003	0.0019	153.2547	0.4416
15.44	0.2249	0.0034	0.0009	0.0022	153.2996	0.4909
16.98	0.2336	0.0034	0.0007	0.0022	152.9260	0.4679
18.68	0.2324	0.0035	0.0004	0.0022	151.6540	0.4890
20.55	0.2559	0.0037	0.0047	0.0024	151.6540	0.4760
22.60	0.2545	0.0063	-0.0122	0.0041	149.2091	0.8134
24.86	0.2545	0.0037	-0.0055	0.0024	150.8761	0.4807
27.35	0.2737	0.0091	0.0067	0.0062	150.8761	1.1101

Table 1. Kinematic data of IC 1459 (major axis)

Radius	v (km/s)	e_v	σ (km/s)	e_σ	h_3	e_h3	h_4	e_h4
-89.608	95.698	25.135	169.480	24.391	-0.068	0.133	0.133	0.133
-75.794	102.597	19.720	163.257	16.297	-0.079	0.106	0.241	0.107
-65.327	121.165	17.883	183.567	22.703	-0.199	0.094	0.239	0.094
-58.974	76.006	16.481	234.049	15.407	-0.019	0.058	0.069	0.063
-53.963	61.948	14.635	241.966	13.329	0.007	0.049	0.075	0.054
-49.787	81.218	13.897	231.859	12.874	-0.032	0.050	0.075	0.054
-46.163	110.24	15.757	262.035	13.837	0.018	0.046	0.080	0.054
-42.810	124.364	13.676	242.944	12.458	-0.057	0.046	0.071	0.051
-39.725	66.984	13.232	255.728	14.135	0.024	0.041	-0.015	0.048
-37.223	67.771	14.594	278.077	12.821	0.028	0.039	0.076	0.048
-34.981	48.423	13.359	270.989	12.674	0.065	0.038	0.030	0.044
-32.739	56.906	10.967	258.893	10.091	0.005	0.033	0.058	0.038
-30.785	38.417	12.847	267.527	11.879	0.002	0.036	0.051	0.043
-29.112	69.605	12.108	268.088	10.983	0.024	0.034	0.060	0.040
-27.428	61.859	13.102	275.242	12.066	-0.010	0.035	0.050	0.042
-25.748	52.271	12.670	274.420	12.825	0.014	0.034	-0.001	0.041
-24.355	70.152	14.619	287.086	13.682	-0.003	0.037	0.040	0.045
-23.234	35.261	12.820	279.566	11.885	0.038	0.034	0.044	0.041
-22.114	20.275	11.958	266.581	11.656	0.003	0.034	0.024	0.040
-20.994	19.439	12.491	280.641	11.685	-0.004	0.033	0.041	0.039
-19.873	21.448	10.453	291.712	9.357	0.024	0.026	0.066	0.032
-18.753	30.122	12.012	286.600	11.272	0.031	0.031	0.037	0.037
-17.634	36.696	10.995	283.593	10.608	0.017	0.028	0.022	0.034
-16.513	20.862	11.180	301.964	10.874	0.059	0.027	0.011	0.032
-15.680	12.527	12.161	308.807	12.062	0.020	0.027	0.008	0.033
-15.120	18.488	13.908	302.048	13.638	0.063	0.033	0.005	0.040
-14.560	0.628	16.895	305.528	17.641	0.054	0.040	-0.037	0.048
-14.000	20.766	12.372	293.623	12.266	0.020	0.030	0.005	0.036
-13.440	22.538	11.843	289.379	11.235	0.027	0.030	0.031	0.036
-12.880	18.442	14.275	312.678	13.395	0.040	0.032	0.045	0.041
-12.320	13.073	13.877	309.492	14.580	0.026	0.031	-0.034	0.038
-11.760	20.24	12.140	318.476	11.560	0.042	0.026	0.039	0.034
-11.200	7.132	13.393	310.274	12.989	0.058	0.031	0.016	0.037
-10.640	11.204	12.971	308.312	11.974	0.075	0.031	0.044	0.038
-10.080	1.964	11.344	316.647	10.728	0.050	0.025	0.040	0.032
-9.520	14.763	11.508	308.410	10.749	0.042	0.026	0.045	0.033
-8.960	-11.319	10.450	307.970	9.865	0.065	0.024	0.032	0.030
-8.400	2.195	11.973	315.360	11.706	0.052	0.027	0.015	0.033
-7.840	-0.192	11.165	326.330	11.215	0.081	0.024	-0.011	0.029
-7.280	-11.324	10.741	315.678	9.805	0.053	0.024	0.063	0.031
-6.720	-14.223	11.613	322.202	11.122	0.093	0.026	0.018	0.031
-6.160	-18.614	11.714	341.184	11.177	0.067	0.024	0.052	0.031
-5.600	-19.66	12.040	338.357	11.596	0.091	0.026	0.029	0.031
-5.040	-32.463	11.824	341.004	11.608	0.077	0.024	0.025	0.030
-4.480	-44.091	11.259	338.169	10.803	0.104	0.025	0.023	0.029
-3.920	-50.476	11.266	334.689	10.751	0.097	0.025	0.029	0.030
-3.360	-51.924	11.881	338.544	11.498	0.089	0.025	0.027	0.031
-2.800	-59.817	10.187	330.681	9.706	0.104	0.023	0.022	0.027
-2.240	-56.934	10.723	341.247	10.165	0.117	0.024	0.027	0.028
-1.680	-56.246	11.498	346.636	10.854	0.101	0.024	0.048	0.030
-1.120	-34.563	12.155	343.103	11.845	0.076	0.025	0.034	0.031
-0.560	-11.207	13.910	341.779	13.939	0.077	0.029	0.009	0.034

Table 2. Kinematic data of IC 1459 (major axis, continued)

Radius	v (km/s)	e_v	σ (km/s)	e_σ	h_3	e_h3	h_4	e_h4
0.000	0.000	13.584	335.607	13.451	0.059	0.028	0.021	0.035
0.560	64.773	13.550	330.543	13.831	-0.019	0.027	0.003	0.034
1.120	41.025	12.329	327.415	12.543	-0.029	0.025	0.001	0.031
1.680	72.978	12.977	324.131	13.110	-0.010	0.027	0.006	0.033
2.240	93.515	13.384	317.287	13.243	-0.022	0.029	0.014	0.036
2.800	88.161	12.975	315.420	12.818	-0.051	0.029	0.008	0.035
3.360	94.115	13.326	319.895	13.020	-0.059	0.029	0.017	0.036
3.920	83.247	13.626	311.288	13.196	-0.052	0.031	0.020	0.038
4.480	77.888	12.533	311.528	12.755	-0.016	0.028	-0.008	0.034
5.040	50.191	13.194	319.595	13.135	-0.006	0.028	0.013	0.035
5.600	57.395	13.182	321.551	13.124	-0.007	0.028	0.015	0.035
6.160	30.099	12.318	311.903	12.207	-0.018	0.027	0.010	0.034
6.720	45.402	11.682	315.057	11.229	0.031	0.026	0.032	0.032
7.280	49.54	11.678	320.937	11.378	0.020	0.025	0.028	0.031
7.840	38.143	11.796	309.733	11.779	0.016	0.026	0.004	0.032
8.400	50.055	13.290	316.146	12.994	0.053	0.029	0.015	0.036
8.960	48.897	13.160	327.410	13.156	0.037	0.027	0.013	0.034
9.520	27.645	12.004	306.298	12.232	0.022	0.027	-0.012	0.033
10.080	14.984	11.952	311.881	11.556	0.043	0.027	0.023	0.033
10.640	17.1	11.947	303.106	11.402	0.063	0.028	0.023	0.034
11.200	18.861	11.859	316.752	12.039	0.033	0.026	-0.006	0.031
11.760	2.951	11.570	316.747	11.553	0.046	0.025	0.003	0.031
12.320	10.752	12.174	311.036	12.311	0.028	0.027	-0.005	0.033
12.880	-4.117	10.728	301.099	10.872	0.046	0.025	-0.013	0.031
13.440	-7.849	10.265	302.861	9.980	0.040	0.024	0.016	0.029
14.000	-1.452	12.259	316.277	12.168	0.020	0.026	0.012	0.033
14.560	-0.432	11.647	305.249	11.583	0.016	0.026	0.005	0.032
15.120	-3.782	13.528	314.441	12.288	0.052	0.031	0.066	0.040
15.680	15.954	10.125	304.898	10.658	0.050	0.024	-0.042	0.029
16.240	2.923	12.771	296.385	12.075	0.045	0.031	0.031	0.038
17.073	-3.435	10.380	301.319	9.704	0.043	0.025	0.040	0.030
18.194	-16.026	10.976	299.967	10.196	0.046	0.026	0.043	0.032
19.314	-26.115	10.609	302.258	9.316	0.055	0.026	0.080	0.033
20.436	-27.453	12.201	308.059	11.141	0.068	0.029	0.054	0.036
21.551	-28.393	12.007	303.493	10.798	0.055	0.029	0.064	0.036
22.674	-33.819	10.082	292.630	8.810	0.084	0.026	0.072	0.032
23.795	-41.113	11.382	294.164	10.656	0.090	0.029	0.025	0.034
24.915	-33.013	12.538	298.468	11.986	0.039	0.030	0.026	0.037
27.988	-36.619	12.789	287.368	11.879	0.040	0.033	0.042	0.039
29.669	-42.04	10.953	297.999	10.392	0.076	0.027	0.022	0.032
31.350	-33.386	11.511	300.428	10.263	0.096	0.029	0.058	0.035
33.303	-46.175	10.867	277.943	10.008	0.045	0.029	0.047	0.035
35.541	-48.5	12.146	275.367	11.475	0.106	0.036	0.019	0.040
37.782	-61.208	11.763	273.917	10.507	0.049	0.033	0.065	0.039
40.294	-57.907	12.915	260.229	11.573	0.106	0.041	0.058	0.045
43.106	-76.088	9.915	234.690	9.735	0.032	0.035	0.045	0.038
46.136	-54.036	11.510	234.418	12.348	0.085	0.043	-0.004	0.047
49.795	-51.694	13.862	255.001	11.893	0.097	0.045	0.091	0.051
53.928	-89.869	14.058	200.652	26.597	0.238	0.071	0.177	0.069
58.963	-97.594	15.891	199.162	27.492	0.158	0.075	0.173	0.075
65.327	-120.835	17.883	183.567	22.703	0.199	0.094	0.239	0.094
73.939	-82.389	23.726	135.026	32.675	0.007	0.142	0.522	0.148
86.244	-108.638	37.625	118.830	69.486	-0.020	0.247	0.398	0.234

Table 3. Kinematic data of IC 3370 (major axis)

Radius	v (km/s)	e_v	σ (km/s)	e_σ	h_3	e_{h_3}	h_4	e_{h_4}
-118.709	-97.283	33.982	108.359	47.825	-0.102	0.306	-0.009	0.346
-76.994	-98.17	13.729	149.995	15.174	-0.020	0.082	0.054	0.088
-58.261	-108.416	13.138	172.560	12.817	0.040	0.065	0.070	0.068
-46.710	-131.07	10.158	157.412	11.417	0.093	0.060	0.023	0.064
-38.513	-118.186	9.072	161.628	10.925	0.077	0.052	-0.015	0.058
-31.791	-111.942	9.111	152.370	10.386	0.086	0.056	0.027	0.059
-26.880	-148.232	10.553	138.989	16.823	0.072	0.080	-0.138	0.112
-23.520	-97.746	9.498	157.489	10.566	0.043	0.054	0.035	0.058
-20.160	-94.81	10.537	186.111	11.442	0.047	0.048	0.000	0.051
-16.800	-77.852	10.333	183.333	9.788	0.047	0.048	0.066	0.049
-13.440	-82.048	10.792	193.314	11.130	0.033	0.046	0.015	0.048
-10.080	-70.944	9.994	189.044	9.632	0.036	0.044	0.050	0.045
-6.720	-69.167	11.289	205.146	10.671	0.007	0.044	0.041	0.045
-3.360	-60.06	11.441	208.147	10.757	0.011	0.044	0.040	0.045
0.000	0.000	11.151	208.537	10.793	0.050	0.043	0.025	0.044
3.360	67.06	10.770	199.582	10.236	0.026	0.044	0.044	0.045
6.720	96.202	11.002	199.779	11.602	-0.028	0.045	-0.001	0.048
10.080	113.86	10.915	204.124	10.313	-0.041	0.043	0.041	0.044
13.440	114.294	9.822	185.917	10.724	-0.024	0.045	0.000	0.048
16.800	125.151	9.606	185.910	11.544	-0.038	0.045	-0.045	0.051
20.160	127.636	9.426	181.309	11.575	-0.013	0.045	-0.047	0.052
23.520	127.365	8.849	170.744	10.957	-0.059	0.047	-0.041	0.054
26.880	129.717	9.302	168.540	11.390	-0.023	0.049	-0.028	0.056
30.240	139.625	9.165	156.671	12.257	-0.092	0.058	-0.066	0.068
35.141	133.451	8.889	148.509	10.985	-0.010	0.055	0.005	0.062
41.864	121.188	8.819	146.365	12.311	0.008	0.057	-0.051	0.071
50.100	146.844	8.659	154.099	12.364	-0.034	0.054	-0.083	0.069
61.694	135.349	9.836	145.376	14.707	0.033	0.067	-0.091	0.088
79.294	122.278	12.685	124.982	15.916	0.073	0.097	0.033	0.104
116.432	124.591	18.182	99.847	30.532	0.093	0.184	-0.102	0.247

Table 4. Kinematic data of IC 3370 (minor axis)

Radius	v (km/s)	e_v	σ (km/s)	e_σ	h_3	e_{h_3}	h_4	e_{h_4}
-80.156	41.732	15.472	185.858	20.348	-0.170	0.103	-0.305	0.149
-61.574	30.78	17.496	233.660	11.910	-0.133	0.065	0.170	0.068
-50.043	54.865	15.371	183.722	13.351	-0.067	0.071	0.107	0.073
-41.662	1.02	21.828	201.291	20.062	-0.058	0.089	0.057	0.091
-35.373	29.818	19.630	232.101	18.222	-0.243	0.093	-0.038	0.080
-30.240	34.231	14.851	186.155	13.909	-0.105	0.070	0.062	0.070
-26.880	21.567	14.278	182.174	11.897	0.016	0.065	0.133	0.068
-23.520	40.021	14.302	183.965	12.714	0.056	0.066	0.096	0.067
-20.160	48.205	15.211	230.440	16.886	0.035	0.052	-0.050	0.057
-16.800	37.463	15.702	216.157	17.973	-0.020	0.058	-0.051	0.065
-13.440	35.915	13.037	205.530	15.336	-0.081	0.056	-0.064	0.061
-10.080	36.775	15.706	220.740	18.126	-0.078	0.061	-0.070	0.067
-6.720	34.023	12.548	216.791	13.353	0.033	0.046	-0.020	0.049
-3.360	35.387	12.093	206.551	12.634	0.025	0.047	-0.002	0.050
0.000	0.000	11.312	223.119	10.956	0.072	0.041	0.011	0.041
3.360	-15.449	11.714	216.859	10.655	0.043	0.043	0.047	0.044
6.720	-32.512	11.494	208.624	11.032	0.038	0.044	0.032	0.045
10.080	-52.446	10.533	193.031	10.462	0.051	0.046	0.033	0.047
13.440	-45.915	11.340	202.402	12.168	-0.040	0.046	-0.011	0.049
16.800	-54.17	11.744	188.615	12.172	-0.051	0.053	0.019	0.055
20.160	-38.137	14.072	213.722	15.152	-0.073	0.055	-0.028	0.057
23.520	-40.025	15.812	210.258	15.055	-0.002	0.060	0.035	0.062
26.880	-78.507	13.215	178.116	13.214	0.035	0.063	0.051	0.066
30.240	-44.075	21.753	245.018	17.623	0.011	0.067	0.079	0.070
35.131	-52.099	13.435	181.799	13.803	0.070	0.064	0.030	0.066
41.859	-32.566	14.869	201.688	14.593	0.076	0.062	0.025	0.063
50.024	-42.578	14.372	174.449	13.211	0.020	0.070	0.098	0.072
62.955	6.104	17.907	212.082	19.989	0.084	0.073	-0.046	0.077
87.898	-14.423	17.562	156.723	22.006	-0.072	0.106	-0.024	0.120

Table 5. Kinematic data of IC 3370 (intermediate axis)

Radius	v (km/s)	e_v	σ (km/s)	e_σ	h_3	e_h3	h_4	e_h4
-59.788	-97.318	11.334	180.295	16.307	0.052	0.059	-0.142	0.082
-46.693	-103.027	9.992	133.376	11.399	0.006	0.068	0.069	0.072
-38.494	-103.169	10.171	147.593	14.390	-0.018	0.066	-0.062	0.083
-31.754	-100.368	9.884	157.162	12.581	0.079	0.060	-0.037	0.068
-26.880	-99.208	10.273	166.574	14.369	0.027	0.057	-0.095	0.074
-23.520	-102.625	10.907	156.696	13.198	0.038	0.063	-0.004	0.071
-20.160	-87.717	10.239	162.518	14.397	0.064	0.061	-0.100	0.077
-16.800	-84.928	10.636	174.007	14.551	0.078	0.059	-0.107	0.073
-13.440	-87.972	10.301	170.535	12.116	0.051	0.054	-0.016	0.059
-10.080	-81.43	9.921	169.085	11.912	0.061	0.053	-0.025	0.059
-6.720	-74.647	10.695	173.391	12.346	0.053	0.055	-0.012	0.060
-3.360	-47.07	11.336	190.177	12.093	0.047	0.050	0.002	0.053
0.000	0.000	11.413	198.156	12.091	0.077	0.049	-0.008	0.051
3.360	48.517	10.996	196.522	13.149	0.021	0.047	-0.053	0.054
6.720	94.703	10.941	188.287	12.965	-0.019	0.049	-0.040	0.056
10.080	107.835	10.712	183.460	13.909	-0.019	0.051	-0.078	0.063
13.440	115.963	10.342	185.005	13.115	-0.036	0.049	-0.069	0.058
16.800	132.163	9.937	176.510	13.251	-0.002	0.050	-0.082	0.063
20.160	133.392	9.804	175.128	13.410	-0.053	0.052	-0.100	0.066
23.520	129.282	9.888	169.665	14.142	-0.083	0.058	-0.134	0.076
26.880	128.456	9.650	169.223	14.866	-0.017	0.056	-0.177	0.084
31.771	139.59	9.432	159.740	14.169	-0.005	0.057	-0.129	0.080
38.494	139.441	9.034	142.028	11.807	-0.149	0.067	-0.047	0.074
46.683	140.017	10.226	150.049	14.515	-0.091	0.069	-0.089	0.086
59.581	134.721	12.377	163.816	15.429	-0.152	0.079	-0.067	0.085
84.130	115.096	12.181	144.219	17.536	-0.150	0.094	-0.128	0.116

Table 6. Kinematic data of NGC 3379 (major axis)

Radius	v (km/s)	e_v	σ (km/s)	e_σ	h_3	e_h3	h_4	e_h4
-25.879	63.194	8.513	162.073	7.368	-0.090	0.045	0.109	0.046
-14.051	68.302	7.637	179.704	7.898	-0.073	0.036	0.028	0.037
-8.753	56.908	4.830	176.622	5.180	-0.012	0.023	0.022	0.024
-6.255	52.234	5.303	183.786	5.603	0.015	0.024	0.024	0.025
-4.809	51.106	5.572	199.728	5.931	-0.015	0.023	0.014	0.024
-3.624	42.337	5.403	207.183	5.545	0.002	0.021	0.026	0.022
-2.773	45.139	5.834	214.089	5.978	-0.011	0.022	0.023	0.023
-2.183	39.724	5.935	219.934	5.964	-0.019	0.021	0.029	0.023
-1.593	35.234	5.928	225.600	6.096	-0.010	0.021	0.016	0.022
-1.003	29.393	5.767	224.304	5.916	-0.003	0.020	0.018	0.022
-0.413	19.156	5.681	217.610	5.945	0.016	0.021	0.012	0.022
-0.177	5.516	5.703	223.417	6.094	0.013	0.020	0.001	0.022
0.767	-3.167	5.601	217.749	5.619	0.016	0.020	0.030	0.022
1.357	-9.204	5.750	208.990	5.938	0.024	0.022	0.022	0.023
1.947	-11.184	6.080	203.897	6.422	0.040	0.024	0.013	0.026
2.798	-18.15	5.505	201.697	5.764	0.028	0.022	0.019	0.023
3.983	-24.77	5.559	196.204	5.828	0.032	0.023	0.021	0.024
5.428	-29.387	5.263	184.628	5.622	0.010	0.023	0.020	0.025
7.704	-30.205	4.881	175.466	5.150	0.025	0.023	0.028	0.024
12.261	-45.279	5.224	171.950	5.111	0.027	0.025	0.060	0.026
20.582	-60.748	7.666	155.531	8.560	0.033	0.042	0.011	0.043

Table 7. Kinematic data of NGC 4105 (major axis)

Radius	v (km/s)	e_v	σ (km/s)	e_σ	h_3	e_{h_3}	h_4	e_{h_4}
-22.585	31.695	62.504	260.281	84.348	0.134	0.246	-0.143	0.310
-14.673	4.87	33.698	234.433	42.807	0.095	0.136	-0.051	0.154
-10.619	35.136	23.159	253.402	27.209	0.072	0.081	-0.026	0.090
-8.165	12.979	19.660	259.904	21.912	0.069	0.066	-0.008	0.071
-6.519	24.065	17.210	262.390	18.105	0.016	0.055	0.020	0.058
-5.356	27.889	14.490	262.859	17.444	0.027	0.047	-0.039	0.055
-4.347	20.754	14.195	257.176	15.235	-0.010	0.047	0.017	0.050
-3.520	11.619	15.405	285.667	17.093	0.021	0.044	-0.021	0.049
-2.847	21.285	14.241	284.228	15.041	0.025	0.041	0.001	0.044
-2.173	15.245	14.320	283.497	14.142	0.027	0.041	0.031	0.043
-1.680	10.452	16.009	310.394	16.202	-0.001	0.040	0.004	0.044
-1.344	4.165	15.589	307.387	15.176	0.032	0.040	0.022	0.042
-1.008	3.815	16.464	298.603	18.045	0.055	0.045	-0.028	0.050
-0.672	7.031	16.050	298.183	16.030	-0.003	0.042	0.017	0.046
-0.336	15.546	14.806	304.751	16.300	-0.022	0.039	-0.030	0.044
0.000	0.000	14.837	298.764	18.337	-0.020	0.041	-0.079	0.051
0.336	1.583	17.086	313.825	18.558	-0.039	0.043	-0.031	0.049
0.672	-5.221	15.298	306.415	16.960	-0.044	0.040	-0.037	0.046
1.008	14.739	15.538	308.173	15.828	-0.067	0.041	-0.003	0.044
1.344	28.992	15.082	285.592	14.677	-0.013	0.042	0.036	0.045
1.680	28.555	15.058	299.200	17.439	-0.058	0.042	-0.054	0.049
2.016	4.331	16.399	301.758	18.116	-0.026	0.043	-0.030	0.049
2.352	50.178	14.001	278.795	16.299	0.001	0.042	-0.036	0.048
2.688	32.482	13.129	254.500	13.943	-0.020	0.044	0.023	0.046
3.181	38.352	13.591	277.016	14.385	0.043	0.041	0.004	0.044
3.855	21.539	14.533	295.552	16.118	-0.029	0.040	-0.028	0.045
4.528	28.619	14.184	273.435	16.533	-0.032	0.044	-0.034	0.050
5.356	41.094	15.362	280.693	16.450	-0.001	0.045	-0.001	0.049
6.516	26.132	14.800	261.816	17.802	0.032	0.049	-0.038	0.056
8.017	31.639	17.392	279.589	19.685	0.032	0.052	-0.026	0.058
9.996	31.828	18.018	262.988	21.318	0.045	0.059	-0.033	0.067
12.943	40.285	25.093	262.602	27.882	0.075	0.083	-0.010	0.089
18.002	66.794	33.495	249.708	45.852	0.014	0.120	-0.085	0.154
27.268	49.384	45.562	248.060	63.312	0.018	0.166	-0.092	0.216

Table 8. Kinematic data of NGC 4105 (minor axis)

Radius	v (km/s)	e_v	σ (km/s)	e_σ	h_3	e_{h_3}	h_4	e_{h_4}
-9.613	66.253	56.865	287.610	63.660	-0.164	0.240	-0.404	0.377
-6.800	-11.076	27.873	243.361	32.630	0.106	0.106	-0.024	0.114
-5.167	41.767	37.886	309.688	28.733	0.076	0.099	0.139	0.105
-4.009	22.206	24.338	283.535	34.077	0.001	0.075	-0.136	0.109
-3.180	9.865	28.872	315.807	26.594	0.044	0.071	0.041	0.075
-2.504	25.53	15.694	288.956	15.782	-0.036	0.044	0.018	0.047
-2.016	25.516	18.632	284.057	22.655	0.073	0.057	-0.070	0.068
-1.680	68.354	23.839	327.022	16.758	0.100	0.060	0.175	0.066
-1.344	2.133	16.576	303.480	16.686	-0.044	0.043	0.008	0.047
-1.008	11.083	18.115	317.555	19.687	0.075	0.046	-0.041	0.052
-0.672	14.812	14.372	288.949	13.448	-0.047	0.040	0.049	0.042
-0.336	-7.478	15.040	318.497	13.816	-0.052	0.037	0.040	0.039
0.000	0.000	14.757	303.940	15.209	0.015	0.038	0.000	0.042
0.336	-3.794	15.515	312.880	13.146	-0.034	0.039	0.082	0.041
0.672	-5.044	19.103	327.555	17.912	-0.008	0.044	0.030	0.048
1.008	-13.082	17.626	301.887	15.988	-0.019	0.046	0.057	0.048
1.344	-31.054	15.749	277.036	16.262	0.006	0.046	0.017	0.049
1.680	-30.863	17.706	305.189	19.507	0.005	0.046	-0.030	0.052
2.169	-7.328	24.048	292.992	18.893	-0.001	0.066	0.133	0.069
2.844	-55.537	53.998	238.476	26.755	0.057	0.277	0.760	0.297
3.668	-5.908	17.948	280.591	24.505	-0.008	0.055	-0.115	0.076
4.829	16.595	19.588	267.684	23.580	0.046	0.063	-0.045	0.073
6.466	58.218	30.208	278.722	34.763	-0.070	0.093	-0.039	0.104
9.289	14.762	67.459	223.187	108.529	0.019	0.327	-0.293	0.556